RSC Advances

PAPER

View Article Online
View Journal | View Issue

Cite this: *RSC Adv.*, 2016, **6**, 79688

Cobalt ferrite nanoparticles *via* a template-free hydrothermal route as an efficient nano-adsorbent for potential textile dye removal

Mostafa Y. Nassar* and Mai Khatab

We have reported herein the preparation of a pure cobalt ferrite ($CoFe_2O_4$) nanostructure, as an efficient nano-adsorbent, *via* a template-free hydrothermal and post thermal conversion route. We prepared micro-spherical particles of a cobalt carbonate/iron carbonate ($CoCO_3/FeCO_3$) composite precursor using the hydrothermal reaction of cobalt sulfate, iron sulfate, ascorbic acid, and ammonium carbonate at 140 °C for 3 h. Various parameters influencing the hydrothermal reaction have been studied. Thermal decomposition of the carbonate composite precursors prepared using different Co^{2+} : Fe^{2+} molar ratios generated various impure products. However, the $CoCO_3/FeCO_3$ composite precursor synthesized employing a $0.4Co^{2+}$: $0.6Fe^{2+}$ molar ratio produced a pure spinel $CoFe_2O_4$ nanostructure with an average crystallite size of 9.5–21.6 nm on calcination in the temperature range of 400–600 °C for 2 h. The products were identified using X-ray diffraction (XRD), field emission scanning electron microscopy (FE-SEM), Fourier transform infrared spectroscopy (FT-IR), high resolution transmission electron microscopy (HR-TEM), nitrogen physical adsorption (BET), zeta potential and thermal analysis. The as-prepared spinel $CoFe_2O_4$ product showed a high adsorption capacity (91.7 mg g^{-1}) toward Reactive Red 195 (RR195) dye in 20 min. The adsorption results fitted well the pseudo-second-order kinetics and could be well described by the Langmuir isotherm model. The RR195 dye adsorption was spontaneous, exothermic, and a physisorption process, implied from the calculated thermodynamic constants: ΔG^0 (from −0.022 to −0.711 kJ mol^{-1}), and ΔH^0 (−7.55 kJ mol^{-1}). It is concluded that the suggested $CoFe_2O_4$ nanostructure can be employed as an efficient nano-adsorbent for the removal of RR195 textile dye from aqueous solutions.

Received 17th May 2016
Accepted 19th August 2016

DOI: 10.1039/c6ra12852a

www.rsc.org/advances

1. Introduction

Recently, magnetic nanostructures have aroused keen interest from a great number of scientists due to the physical and chemical characteristics that these nanomaterials have, compared with the corresponding bulk materials.[1–3] Furthermore, ferrites (MFe_2O_4; M = Co, Zn, Mn, Cu, or Ni) are of great importance to materials science and inorganic material researchers because of their chemical stability and promising electromagnetic characteristics.[4–6] Thus, several methods such as mechanical milling,[7] sol–gel,[8] hydrothermal,[9] micro-emulsion,[10] reverse micelle,[11] co-precipitation,[12] and ultrasonic-assisted hydrothermal processes[13] have been suggested to prepare various ferrite nanostructures.

Cobalt ferrite ($CoFe_2O_4$) is an important member of the spinel ferrite family attributing to the special properties it has such as chemical stability, high mechanical stability, wear resistance, high anisotropy, and moderate saturation magnetization.[14] Therefore, cobalt ferrite can be applied for different applications such as magnetic resonance imaging, drug delivery, catalysis, recording media, gas sensors, ferrofluids, microwave devices, and adsorption.[6,15] Hence, cobalt ferrite nanostructures have been produced *via* various procedures such as sol–gel,[8] electro-spinning,[16] hydrothermal, atomic layer deposition,[17] co-precipitation,[18,19] combustion,[15] and micro-emulsion method.[20] However, the hydrothermal procedure is still one of the most appropriate methods in this respect because of its simplicity, inexpensive cost, and availability to tune the morphology and particle size of the product.[21,22] Recently, employing metal carbonates *via* their thermal decomposition to generate metal oxides is a promising route, and this approach has attracted the attention of several researchers. Consequently, we have previously reported on the hydrothermal synthesis of $CoCO_3$ and $FeCO_3$ nanostructures and their thermal conversion into Co_3O_4 and α-Fe_2O_3 nanoparticles, respectively.[21,23–25] However, to the best of our knowledge, we have noticed that there is only one report on the synthesis of $CoCO_3/FeCO_3$ composite, and this report has not extensively explored the different parameters influencing the preparation process.[26] This stimulated us to investigate extensively the template-free hydrothermal preparation of $CoCO_3$/

Chemistry Department, Faculty of Science, Benha University, Benha 13518, Egypt. E-mail: m_y_nassar@yahoo.com; m_y_nassar@fsc.bu.eg.edu; Tel: +20 1068727555

$FeCO_3$ composite as a carbonate precursor to produce porous cobalt ferrite nanostructure *via* thermal decomposition.

Meanwhile, environmental pollution with textile dyes generated from various industries including paper, leather, chemical and textile dyeing is a dangerous problem to our world due to the various health difficulties that pollution causes.[27,28] It is known that the organic textile dyes (especially reactive dyes) are carcinogenic and toxic attributing to the azo groups that their chemical structures have.[25,29] Plus, Reactive Red 195 dye (RR195), Scheme 1, is one of these toxic dyes which is stable toward photodegradation.[25] Removal of such discharged organic pollutants from wastewater is still a challenge. Therefore, different procedures have been suggested for solving such problems such as photodegradation, adsorption, *etc.*[30–34] Moreover, adsorption process still has the priority over the others in this concern because of its commercial applicability, high performance, and relatively nontoxic species.[19] Nowadays, ferrites have been proposed as adsorbents due to their magnetic property, mechanical and chemical stability.[6,35,36]

Herein, we have reported a new strategy to synthesize $CoFe_2O_4$ nanostructure as an efficient nano-adsorbent *via* a template-free hydrothermal route. Therefore, $CoCO_3/FeCO_3$ microspheres were synthesized using the hydrothermal reaction of cobalt sulfate, iron sulfate, ascorbic acid, and ammonium carbonate at 140 °C for 3 h, in the absence of any template and special solvent. Notably, the ascorbic acid was used as a reducing agent, and ammonium carbonate was used as an inexpensive carbonate source. Different parameters influencing the hydrothermal reaction were extensively studied including the Co^{2+} : Fe^{2+} molar ratios. Thermal decomposition of the hydrothermally prepared carbonate composites was explored to generate pure spinel cobalt ferrite product. The as-produced cobalt ferrite ($CoFe_2O_4$) nanoparticles revealed good adsorption properties toward the removal of Reactive Red 195 textile dye (RR195) from wastewater.

2. Experimental

2.1. Materials and reagents

The chemicals used in the current research: iron sulfate ($FeSO_4 \cdot 7H_2O$), cobalt sulfate ($CoSO_4 \cdot 7H_2O$), and ascorbic acid ($C_6H_8O_6$), were purchased from Sigma-Aldrich company. Ammonium carbonate ($(NH_4)_2CO_3$) was purchased from Fluka company. Reactive Red 195 dye (RR195) ($C_{31}H_{19}ClN_7O_{19}S_6Na_5$) was purchased from Rushabh chemicals industries, India. All other chemicals were of analytical grade and utilized as received without further purification.

2.2. Preparation of $CoCO_3/FeCO_3$ composite precursor

In a typical synthesis process, under the optimized experimental conditions: an aqueous solution (20 mL) of ammonium carbonate (3.45 g, 35.91 mmol, 3 eq.) was added to a stirring aqueous solution (40 mL) of iron sulfate (2.0 g, 7.18 mmol, 0.6 eq.), ascorbic acid (2.11 g, 11.97 mmol, 1 eq.), and cobalt sulfate (1.35 g, 4.79 mmol, 0.4 eq.). The reaction mixture was stirred for 20 min and transferred into a 100 mL Teflon-lined autoclave. The autoclave was then carefully closed and placed in an oven set at 140 °C for 3 h. Subsequently, the brownish precipitate was isolated by centrifugation after the autoclave was allowed to reach the room temperature naturally. The carbonate composite product was washed with water and ethanol several times and dried in an electric oven at 60 °C overnight. The effect of Co^{2+} : Fe^{2+} molar ratios (0.1 : 0.9, 0.2 : 0.8, 0.3 : 0.7, 0.4 : 0.6, 0.5 : 0.5, 0.6 : 0.4, 0.7 : 0.3, 0.8 : 0.2, and 0.9 : 0.1) on the hydrothermal process was studied, and the products were denoted as S19, S28, S37, S46, S11, S64, S73, S82, and S91, respectively. In addition, the influence of the reaction time (1.5, 3, 6, 12, and 24 h) on the

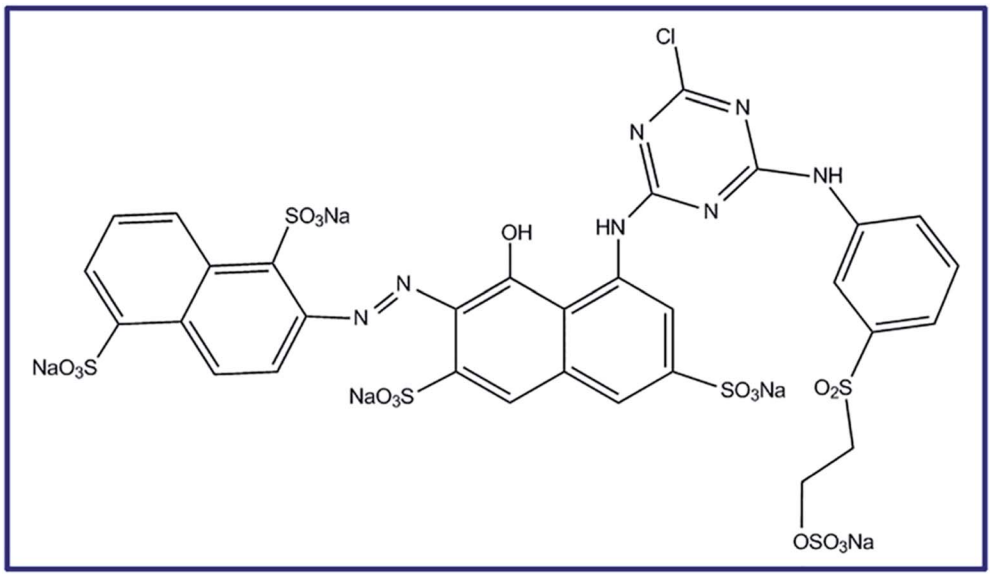

Scheme 1 Reactive Red 195 (RR195) dye molecular structure.

reaction was also investigated for the hydrothermal reaction with $0.4Co^{2+}$: $0.6Fe^{2+}$: 1ascorbic acid : $3CO_3^{2-}$ molar ratio.

2.3. Preparation of cobalt ferrite nanoparticles

Pure spinel cobalt ferrite ($CoFe_2O_4$) nanoparticles: S46_400, S46_500, and S46_600, were produced by calcination of the $CoCO_3/FeCO_3$ composite precursor (S46), prepared using $0.4Co^{2+}$: $0.6Fe^{2+}$ molar ratio, for 2 h at 400, 500 and 600 °C, respectively. This particular molar ratio (*i.e.* $0.4Co^{2+}$: $0.6Fe^{2+}$) was chosen after investigation of the products produced on calcination, at 600 °C for 2 h, of the carbonate composite precursors prepared using various Co^{2+} : Fe^{2+} molar ratios (0.1 : 0.9, 0.3 : 0.7, 0.4 : 0.6, 0.5 : 0.5, 0.7 : 0.3, and 0.9 : 0.1), and the products were referred to as S19_600, S37_600, S46_600, S11_600, S37_600, and S91_600, respectively.

2.4. Characterization

The phase formation of the as-prepared nanostructures and their purity were identified by means of XRD patterns using X-ray diffractometer; Bruker, model D8 Advance, with Cu-Kα radiation; $\lambda = 1.54178$ Å. The surface structure and purity of the as-synthesized products were explored using a field emission scanning electron microscope (FE-SEM; JEOL JSM-6390). A high-resolution transmission electron microscope (HR-TEM; JEM-2100) with an accelerating voltage of 200 kV was employed to investigate the detailed morphology of the as-synthesized products. The Fourier transform infrared spectra were collected in the range of 4000–400 cm^{-1} on FT-IR spectrometer (FT-IR; Thermo Scientific, model Nicolet iS10). A Jasco UV-visible spectrophotometer (UV-Vis; Jasco, model v670) was used to measure the UV-Vis spectra of the Reactive Red 195 dye (RR195) during the adsorption process investigation. Thermal analysis investigation of the as-prepared $CoCO_3/FeCO_3$ composite precursor was performed under N_2 atmosphere using thermal analyzer equipment (Shimadzu; model TA-60WS), and the heating rate of this investigation was 15 °C min^{-1}. Using N_2 vapor adsorption investigation, the BET (Brunauer–Emmett–Teller) surface area of the as-synthesized $CoFe_2O_4$ nanoparticles was performed on Quantachrome (USA; Nova 2000 series). Zeta potential of the as-synthesized $CoFe_2O_4$ nanoparticles was measured at various pH values (from 2 to 10) in 0.01 M NaCl solutions using a Zeta-sizer nano series meter (UK; Malvern, Nano ZS); hence, the isoelectric point (IEP) of the as-synthesized $CoFe_2O_4$ nanostructures was estimated. The chemical stability of the as-prepared $CoFe_2O_4$ nanoparticles was investigated through determination of the concentration of the released cobalt and iron ions in solutions with pH 2, from $CoFe_2O_4$ after 24 and 48 h, using an inductively coupled plasma-optical emission spectrometer (ICP-OES; Optima 7000 DV, PerkinElmer, USA).

2.5. Cell culture and cytotoxicity evaluation

The cytotoxicity of the $CoFe_2O_4$ nanoparticles against normal human fibroblast cell line (MRC-5 cells; obtained from VACSERA, Tissue Culture Unit, Egypt) was evaluated by using MTT assay. All cytotoxicity evaluation experiments were carried out and analyzed by Tissue Culture Unit (The Regional Center for Mycology and Biotechnology, Al-Azhar University, Cairo, Egypt). Cytotoxicity evaluation was performed according to the methods reported by Mosmann[37] and Gomha *et al.*[38]

2.5.1. Cell line propagation. The cells were propagated in Dulbecco's modified Eagle's medium (DMEM) supplemented with 1% L-glutamine, 10% heat-inactivated fetal bovine serum, 50 μg mL^{-1} gentamicin, and HEPES buffer. All cells were maintained at 37 °C in a humidified atmosphere with 5% CO_2 and sub-cultured two times a week during the experimentation.

2.5.2. Cytotoxicity evaluation using the viability assay. The cells were seeded in 96-well plate in a growth medium (100 μL) at a specific cell concentration (1×10^4 cells per cell). After 24 h of seeding, fresh medium having various concentrations of the $CoFe_2O_4$ nanoparticles were added. Using a multichannel pipette, serial two-fold dilutions of the suspended $CoFe_2O_4$ nanoparticles were added to confluent cell monolayers dispensed into 96-well, flat-bottomed microtiter plates. Afterward, the microtiter plates were maintained at 37 °C for 48 h in a humidified incubator with 5% CO_2. Notably, three wells were employed for each concentration of the $CoFe_2O_4$ nanoparticles. The control cells were incubated in the absence of $CoFe_2O_4$ nanoparticles. Different concentrations of the nanomaterial were added to the previously incubated cells, and the incubation was continued for 24 h. Consequently, the viable cells yield was estimated using a colorimetric method. Briefly, after incubation, the media were removed and the number of viable cells were determined using the 1% crystal violet solution as reported by Gomha *et al.*[38] by measuring the absorbance of the plates at a wavelength of 490 nm using a microplate reader (SunRise, TECAN, Inc., USA). All the experiments were performed in triplicate. The percentage of viability (cell viability%) was determined using eqn (1).

$$\text{Cell viability\%} = [1 - (OD_t/OD_c)] \times 100 \quad (1)$$

where, OD_t and OD_c are the mean optical density of the treated wells with $CoFe_2O_4$ nanoparticles, and the mean optical density of the untreated wells, respectively. Plotting of surviving cells against the nanomaterial concentration was achieved to obtain the survival curve of the cell line after its treatment with the nanomaterial of interest. In addition, the 50% cytotoxicity concentration (CC_{50}, the concentration of the nanomaterial required to cause toxic effects in 50% of intact cells) was then determined.

2.6. Adsorption studies

A batch technique was used to investigate the applicability of the as-synthesized $CoFe_2O_4$ nanostructure as an adsorbent for the removal of Reactive Red 195 dye (RR195). Thus, various adsorption experiments were carried out for studying the adsorption of RR195 dye on the as-synthesized $CoFe_2O_4$ adsorbent. Briefly, 0.05 g of the as-synthesized adsorbent was magnetically stirred (430 rpm) with 25 mL of the dye solution of specific pH pre-adjusted using either 0.2 M HCl or 0.2 M NaOH aqueous solutions. After stirring for a pre-defined time (t) (at a specific temperature), an aliquot was withdrawn out of the flask, and the adsorbent

suspension was separated by an external magnet or centrifugation. Using a UV-Vis spectrophotometer, the residual dye concentration (C_t) after adsorption was determined by measuring the absorbance of the supernatant at λ_{max} = 542 nm and employing a pre-constructed calibration curve for the dye of interest. The adsorbed quantity at t time (q_t) and the percentage removal of RR195 dye (%R) could be determined using eqn (2) and (3), respectively.

$$q_t = \frac{V(C_0 - C_t)}{m} \quad (2)$$

$$\%R = \frac{(C_0 - C_t)}{C_0} \times 100 \quad (3)$$

where, C_0 (mg L^{-1}) is the initial dye concentration, C_t (mg L^{-1}) is the final dye concentration in the supernatant, m (g) is the adsorbent mass, V (L) is the dye solution volume, and q_t (mg g^{-1}) is the adsorbent adsorption capacity at time t.

Various experimental parameters influencing the dye adsorption were examined and these parameters included: initial pH of the dye solution (1–10), contact time (5–70) min, effect of potassium chloride (0.05–0.55 g), and temperature (298–328 K). However, for the adsorption isotherm investigation, 0.05 g of the $CoFe_2O_4$ adsorbent was stirred with RR195 dye of different initial concentrations (10–80 mg L^{-1}). The quantity of the adsorbed dye at equilibrium (q_e, mg g^{-1}) was estimated using the following equation:

$$q_e = \frac{V(C_0 - C_e)}{m} \quad (4)$$

where, C_e (mg L^{-1}) is the concentration of the dye in the supernatant solution at equilibrium, and the other terms have the same aforementioned meaning.

3. Results and discussion

3.1. Hydrothermal synthesis and structural investigation of $CoCO_3/FeCO_3$ composite precursors

In our earlier reports, we reported on the hydrothermal preparation of some simple metal carbonates as efficient precursors for producing the corresponding metal oxides by thermal decomposition.[23,25,39] Thus, in the present study, we have employed the hydrothermally prepared $CoCO_3/FeCO_3$ composite precursor to produce a porous spinel $CoFe_2O_4$ nanostructure by thermal conversion. In this connection, we firstly have extensively investigated the hydrothermal reactions of cobalt sulfate, ammonium carbonate, and iron sulfate, in the presence of ascorbic acid as a reducing agent to protect Fe^{2+} from oxidation during the reaction. The as-prepared spinel product was then investigated as an adsorbent for the removal of a textile dye from aqueous solutions.

Fig. 1(a) reveals the XRD reflections of the pure $CoCO_3/FeCO_3$ composite (S46) prepared under the optimized conditions: 0.4Co^{2+} : 0.6Fe^{2+} : 1ascorbic acid : 3CO_3^{2-} molar ratio, at 140 °C, and for 3 h. All the reflections can be well assigned to a mixture of pure rhombohedral phase of cobalt carbonate, which is compatible with the standard XRD pattern of cobalt carbonate (JCPDS card 78-0209; space group $R\bar{3}c$),[23,40] and pure $FeCO_3$ rhombohedral phase, which is in accordance with $FeCO_3$ standard patterns (JCPDS card 83-1764; space group $R\bar{3}c$).[25,41] Other phases corresponding to impurities have not been observed in the XRD patterns. The estimated average crystallite size of the as-prepared $CoCO_3/FeCO_3$ composite nanoparticles, using the Debye–Scherrer eqn (5), was found to be 17.4 nm:[42]

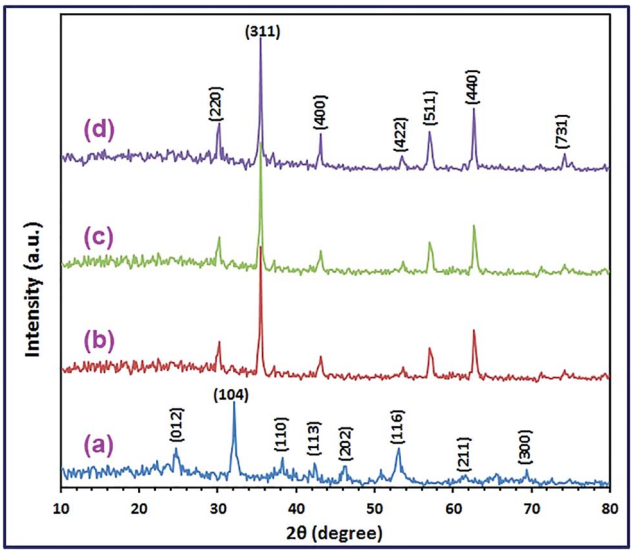

Fig. 1 XRD patterns of the as-synthesized $CoCO_3/FeCO_3$ nanocomposite (a), and $CoFe_2O_4$ products; S46_400 (b), S46_500 (c), and S46_600 (d).

$$D = 0.9\lambda/\beta \cos \theta_B \quad (5)$$

where, D is the crystallite size (nm), λ is the X-ray radiation wavelength (nm), β is the XRD line full width at half maximum (FWHM), and θ_B is the angle of the Bragg diffraction. Afterward, we have fabricated cobalt ferrite nanoparticles ($CoFe_2O_4$) by thermal decomposition of the $CoCO_3/FeCO_3$ composite nanoparticles prepared hydrothermally at the optimized conditions, as will be discussed later. And the XRD patterns of the generated $CoFe_2O_4$ nanoparticles are displayed in Fig. 1(b) and (c).

3.1.1. Optimization of the hydrothermal synthesis of $CoCO_3/FeCO_3$ composite precursor. The effects of Co^{2+} : Fe^{2+} molar ratio and reaction time on the hydrothermal preparation of $CoCO_3/FeCO_3$ composite precursor have been studied. In this reaction, the overall molar ratio of the metal cations was kept equal to 1 equivalent (*i.e.* M^{2+} overall molar ratio = molar ratio of Co^{2+} + molar ratio of Fe^{2+} = 1). Moreover, the overall molar ratio of M^{2+} : ascorbic acid : CO_3^{2-} was remained equal to 1 : 1 : 3, respectively. On the other hand, various Co^{2+} : Fe^{2+} molar ratios (0.1 : 0.9, 0.2 : 0.8, 0.3 : 0.7, 0.4 : 0.6, 0.5 : 0.5, 0.6 : 0.4, 0.7 : 0.3, 0.8 : 0.2, and 0.9 : 0.1) have been investigated. The XRD patterns of the carbonate composite samples (S19, S28, S37, S46, S11, S64, S73, S82, and S91) prepared using the aforementioned Co^{2+} : Fe^{2+} molar ratios, respectively, are displayed in Fig. 2(a)–(i). The XRD results revealed that S19, S37, S46, S11, S73, and S82 samples were pure $CoCO_3/FeCO_3$

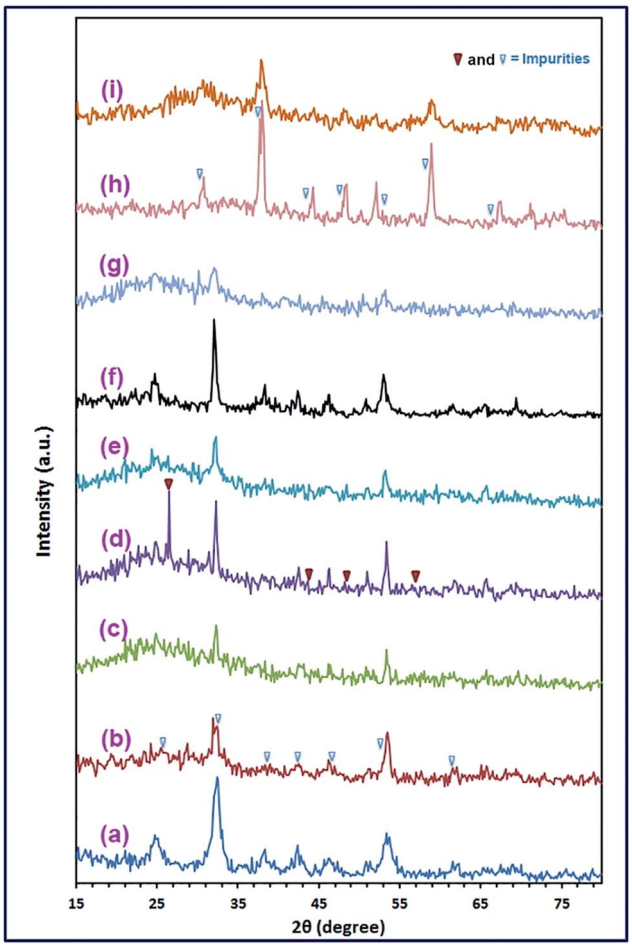

Fig. 2 XRD patterns of the as-synthesized samples; S19 (a), S28 (b), S37 (c), S46 (d), S11 (e), S64 (f), S73 (g), S82 (h), and S91 (i), with Co^{2+} : Fe^{2+} molar ratios of 0.1 : 0.9, 0.2 : 0.8, 0.3 : 0.7, 0.4 : 0.6, 0.5 : 0.5, 0.6 : 0.4, 0.7 : 0.3, 0.8 : 0.2, and 0.9 : 0.1, respectively; under hydrothermal conditions: 140 °C for 3 h.

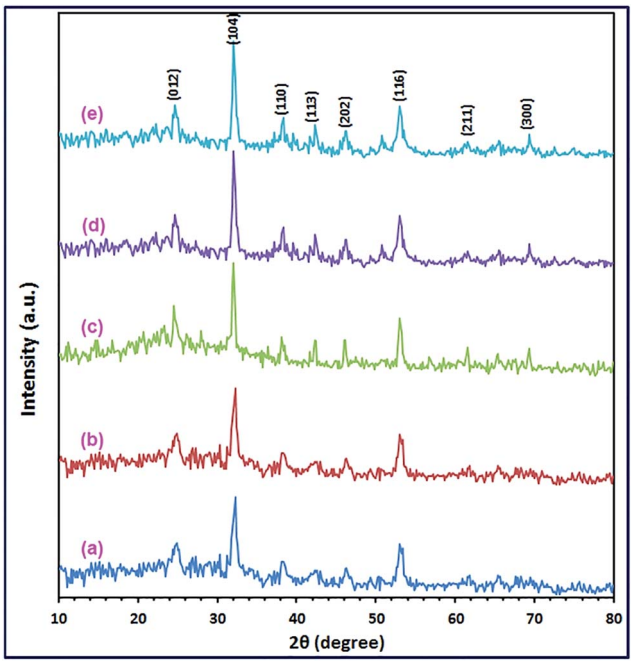

Fig. 3 XRD patterns of the as-synthesized $CoCO_3/FeCO_3$ composites under hydrothermal reactions: Co^{2+} : Fe^{2+} : ascorbic acid : CO_3^{2-} molar ratio of 0.4 : 0.6 : 1 : 3, respectively, at 140 °C, for varying reaction times of 1.5 (a), 3 (b), 6 (c), 12 (d), and 24 h (e).

composite products, while the other samples: S28, S64, and S91, were not.

Moreover, as will be shortly explained in item 3.2., the only sample that produced pure cobalt ferrite product on calcination was S46 which was prepared using $0.4Co^{2+}$: $0.6Fe^{2+}$ molar ratio. Thus, we subsequently have investigated the effect of reaction time (1.5, 3, 6, 12, and 24 h) on the hydrothermal reaction of interest with $0.4Co^{2+}$: $0.6Fe^{2+}$: 1ascorbic acid : $3CO_3^{2-}$ molar ratio at 140 °C. The XRD patterns of the precursor samples are presented in Fig. 3(a)–(e). The results exhibited that 3 h was sufficient to produce pure $CoCO_3/FeCO_3$ composite; consequently, 3 h was chosen as the optimum reaction time for the hydrothermal reaction. Moreover, at reaction times of >3 h, the reaction gave $CoCO_3/FeCO_3$ composite particles with larger crystallite sizes. On the other hand, shorted reaction time yielded poor crystalline carbonate composite.

3.1.2. FE-SEM and TEM investigation. Surface morphology of the $CoCO_3/FeCO_3$ composite precursor (S46) prepared under the optimized conditions was investigated by the FE-SEM spectroscopy. The FE-SEM images, Fig. 4(a) and (b), exhibit that the carbonate composite is composed of a well-dispersed and well-defined spherical shape nanostructure with an average diameter of *ca.* 4 μm, as shown in the low magnification FE-SEM image (Fig. 4(a)). The surfaces of the most spheres are smooth; however, some of the spheres have a rough surface. And the rough surface, as shown in the high magnification image (Fig. 4(b)), is consisted of small cube-like nanostructures. Fig. 4(e) and (f), the TEM images of the as-prepared $CoCO_3/FeCO_3$ composite precursor exhibit the presence of voids in its structure indicating the porous nature of the carbonate composite precursor. Moreover, based on the reported data[21,24,25,43,44] and the obtained morphology, we proposed the formation mechanism of spherical $CoCO_3/FeCO_3$ composite particles as follows. The nucleation and growth mechanism of the $CoCO_3/FeCO_3$ composite crystals can be explained by a precipitation–dissolution–renucleation–growth–aggregation mechanism.[21,45] At the beginning, when the reaction blend solution reaches its supersaturation, initial precipitates are immediately formed. Afterward, this step is followed by dissolution of unstable precipitates leading renucleation and growth of the composite crystallites.[21,46,47] The generated composite crystallites aggregate into final crystals, as explained in mineralization processes.[21,42] Plus, the mechanisms of formation of $CoCO_3$ and $FeCO_3$ have been previously proposed by Nassar *et al.*[24,25] Consequently, the formation mechanism of the $CoCO_3/FeCO_3$ composite can be proposed according to the reactions (i)–(xii) (Scheme 2). Ammonium carbonate serves as a carbonate source. It is reported that at lower concentrations of carbonate, reactions (i), (ii), and (v) through (xii) will be the more predominant reactions generating various products such as $CoCO_3$,

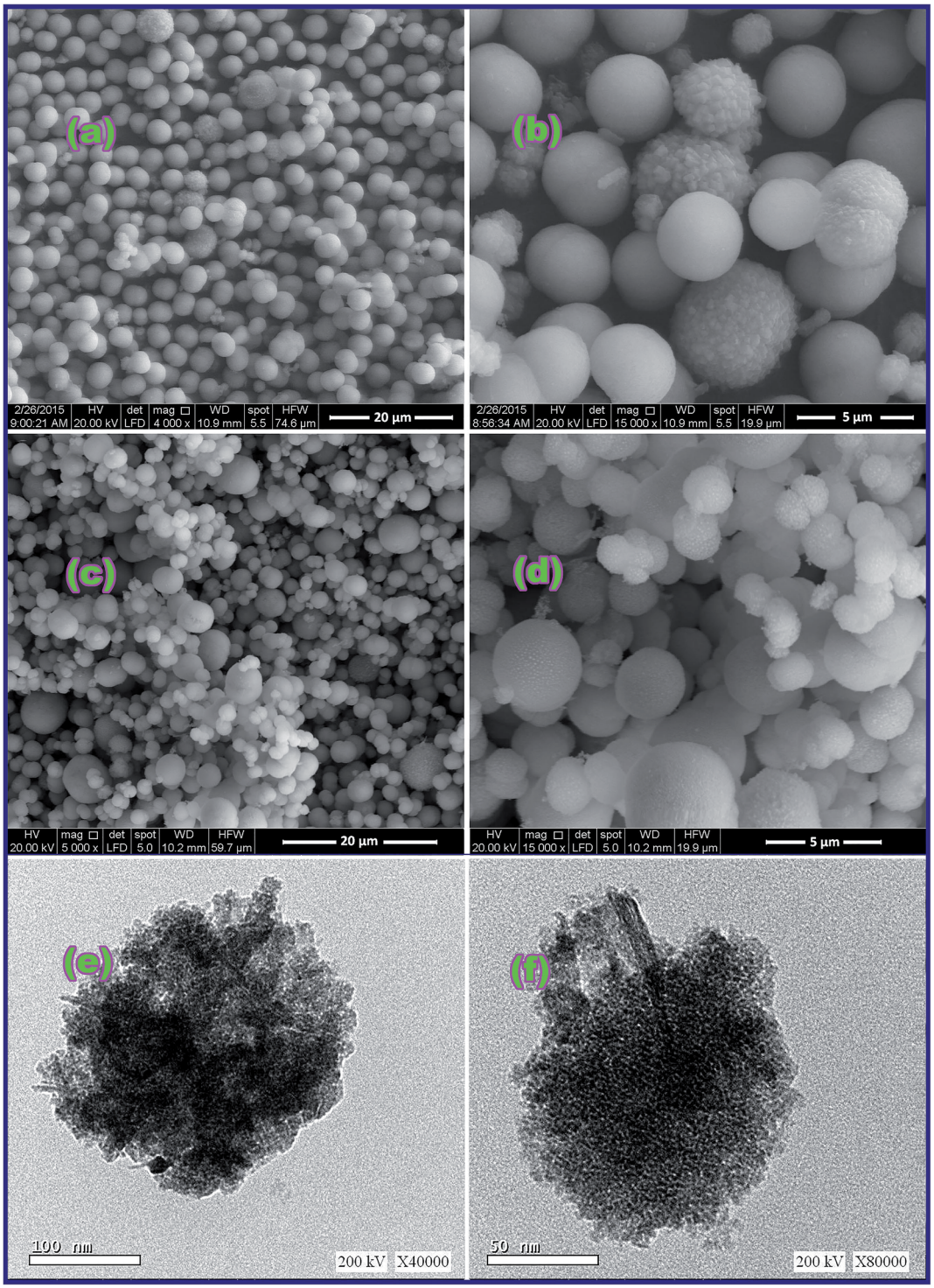

Fig. 4 FE-SEM images of the as-synthesized $CoCO_3/FeCO_3$ nanocomposite (a and b) and $CoFe_2O_4$ product (S46_600 (c and d)); low and high magnification TEM images of $CoCO_3/FeCO_3$ nanocomposite (e and f), respectively. where (a and c) are low magnification FE-SEM images, while (b and d) are high magnification FE-SEM images.

$FeCO_3$, Fe_3O_4, Co_3O_4, and others (Scheme 2). However, at higher carbonate concentrations (*i.e.* ≥3 equivalent, as in our case), reactions (i) through (iv) will be the more predominant reactions producing pure $CoCO_3/FeCO_3$ composite. In addition, the spherical particle morphology of the composite product may be attributed to the non-preferable orientation for the composite crystallites growth.

3.1.3. FT-IR investigation. We employed the FT-IR spectroscopy to further identify the chemical composition of the $CoCO_3/FeCO_3$ composite product (S46) prepared at the optimized

$$(NH_4)_2CO_3 \longrightarrow 2\,NH_4^+ + CO_3^{2-} \quad \text{(i)}$$

$$FeSO_4 + CoSO_4 \longrightarrow Fe^{2+} + Co^{2+} + 2SO_4^{2-} \quad \text{(ii)}$$

$$Fe^{2+} + Co^{2+} + 2CO_3^{2-} \longrightarrow FeCO_3 + CoCO_3 \quad \text{(iii)}$$

$$2\,Fe^{3+} + C_6H_8O_6 \longrightarrow 2\,Fe^{2+} + C_6H_6O_6 + 2H^+ \quad \text{(iv)}$$

$$2\,CO_3^{2-} + 2\,H_2O \longrightarrow 2HCO_3^- + 2\,OH^- \quad \text{(v)}$$

$$Fe^{2+} + 2\,OH^- \longrightarrow Fe(OH)_2 \quad \text{(vi)}$$

$$Fe(OH)_2 + CO_3^{2-} \longrightarrow FeCO_3 + 2OH^- \quad \text{(vii)}$$

$$Fe^{3+} + 3\,OH^- \longrightarrow Fe(OH)_3 \quad \text{(viii)}$$

$$Fe(OH)_2 + Fe(OH)_3 \longrightarrow Fe_3O_4 + 4\,H_2O \quad \text{(ix)}$$

$$Co^{2+} + 2\,OH^- \longrightarrow Co(OH)_2 \quad \text{(x)}$$

$$Co^{2+} + 3\,OH^- \xrightarrow[140\ ^oC,\ 3h]{\text{hydrothermal conditions}} Co(OH)_3 \quad \text{(xi)}$$

$$Co(OH)_2 + 2Co(OH)_3 \xrightarrow[140\ ^oC,\ 3h]{\text{hydrothermal conditions}} Co_3O_4 + 4H_2O \quad \text{(xii)}$$

Scheme 2 Proposed reaction mechanism for the formation of $CoCO_3/FeCO_3$ composite and other compounds.

conditions. The FT-IR spectrum (Fig. 5(a)) exhibits vibrational absorptions; at 1450, 1320, 1040, 858, and 736 cm^{-1}, which can be assigned to $CoCO_3$ with CO_3^{2-} anion D_{3h} symmetry, and this result is in good agreement with the published data.[23,48] Fig. 5(a) also shows vibrations at 1380, 1090, 858, and 736 cm^{-1} corresponding to $FeCO_3$ with CO_3^{2-} anion D_{3h} symmetry in the same sample, and this is consistent with the reported results.[25,48]

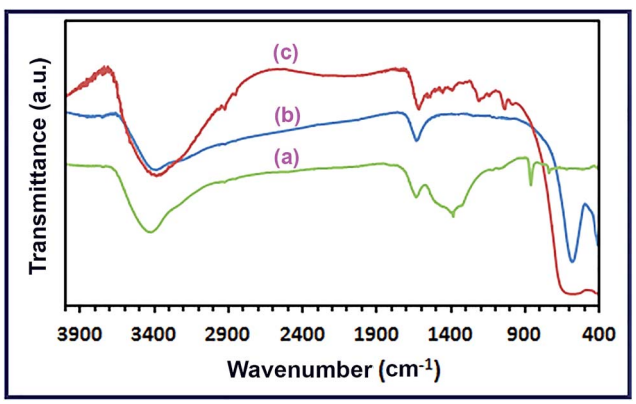

Fig. 5 FT-IR spectra of the as-prepared $CoCO_3/FeCO_3$ nanocomposite (a), spinel $CoFe_2O_4$ (b), and RR195-loaded $CoFe_2O_4$ (c).

However, it is notable that both metal carbonates contributed to the carbonate anion vibrations appeared at 2470, 858, and 736 cm^{-1}. Besides, the spectrum also exhibits a stretching vibration band at *ca.* 2470 cm^{-1} which can be attributed to the carbonate anion vibrational absorption of both $CoCO_3$ and $FeCO_3$. As the FT-IR spectrum confirms the co-existence of cobalt and iron carbonates in the sample (S46), it can be concluded that this product is a mixture of $CoCO_3$ and $FeCO_3$. Therefore, the product (S46) is pure $CoCO_3/FeCO_3$ composite product, and this is consistent with XRD results. It is noteworthy that the FT-IR spectrum of $CoCO_3/FeCO_3$ composite precursor reveals two additional vibrational absorption bands at 3400 and 1630 cm^{-1} corresponding to the stretching and bending vibrations, respectively, of the adsorbed water molecules on the surface of the composite nanoparticles.[48,49]

3.1.4. Thermal properties of the as-prepared $CoCO_3/FeCO_3$ nanocomposite. Thermal properties of the as-prepared $CoCO_3/FeCO_3$ composite using the TG and DTA analyses (Fig. 6) were investigated to further confirm the chemical composition of the $CoCO_3/FeCO_3$ composite precursor (S46). The TG curve (Fig. 6(a)) exhibits three weight loss steps, as outlined in Scheme 3. The first step, within the temperature range of 30–130 °C with a weight loss of 4.85% (calcd 4.88%), corresponds to the

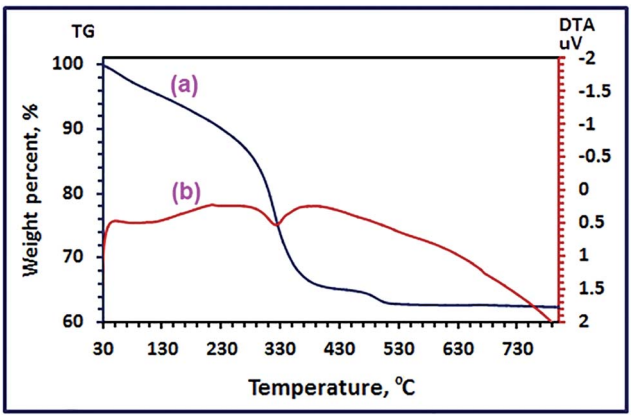

Fig. 6 TG (a), and DTA (b) analyses of the as-prepared $CoCO_3/FeCO_3$ nanocomposite under nitrogen gas.

elimination of the adsorbed water (1 mole of water per each mole of the composite) from the surface of the composite nanoparticles. The second step occurred in the temperature range of 130–432 °C, with a weight loss of 29.94% (calcd 29.97%), could be assigned to a loss of 2 moles of CO_2 and 0.804 mole of CO leaving 0.804 mole of $CoFe_2O_4$ and 0.196 mole of $CoFe_2(O_2)(CO_3)$ as residues. It seems that most of the metal carbonates have completely decomposed, in the second stage, to give $CoFe_2O_4$ (found 50.91%; calcd 51.17%) as a stable product, and the remaining carbonates have thermally converted to $CoFe_2(O_2)(CO_3)$ (found 13.88%; calcd 13.96%). It is worthy to mention that some of the carbonate composite behaved similarly (in its thermal decomposition) to the cobalt carbonate reported by us elsewhere because some of $CoCO_3$ did not give directly Co_3O_4 as a final product on thermal decomposition, but it gave $Co_3(O_2)(CO_3)$ intermediate.[24] Finally, the third weight loss step took place in the temperature range of 432–534 °C with a weight loss of 1.9% (calcd 1.5%) attributing to the decomposition of the intermediate $CoFe_2(O_2)(CO_3)$ (0.196 mole) into $CoFe_2O_4$, 0.196 mole, (found 12.40%; calcd 12.47%) as a final stable product and giving off 0.196 mole of CO. Consequently, the total percentage of the $CoFe_2O_4$ product weight is *ca.* 63.31% which is close to the calculated value (calcd 63.64%). The DTA curve, Fig. 6(b), revealed three endothermic peaks corresponding to the three steps appeared in the TG analysis. The first one appeared at *ca.* 100 °C was broad, and this could be attributed to the loss of the adsorbed water molecules. The second one at 328 °C could be assigned to decomposition of the most of the carbonate composite generation of $CoFe_2O_4$ and $CoFe_2(O_2)(CO_3)$. However, the third DTA peak appeared at *ca.* 490 °C was very broad, and it might be due to the decomposition of the remaining $CoFe_2(O_2)(CO_3)$ intermediate to produce $CoFe_2O_4$.

3.2. Synthesis and characterization of $CoFe_2O_4$ nanoparticles

For the hydrothermal treatment of interest, as various Co^{2+} : Fe^{2+} molar ratios (0.1 : 0.9, 0.3 : 0.7, 0.4 : 0.6, 0.5 : 0.5, 0.7 : 0.3, and 0.9 : 0.1) gave pure $CoCO_3/FeCO_3$ composite products; S19, S37, S46, S11, S73, and S82, respectively, all pure carbonate composite samples were calcined at 600 °C for 2 h. The produced products were denoted as S19_600, S37_600, S46_600, S11_600, S37_600, and S91_600, respectively. The XRD patterns of the calcined products are displayed in Fig. 7(a)–(f). The XRD results revealed that the carbonate composite precursor (S46) produced pure cobalt ferrite product (S46_600) by calcination at 600 °C, as shown in Fig. 7(d) and 1(d). The XRD reflections of the product (S46_600) could be well indexed to the standard XRD pattern of the pure cubic $CoFe_2O_4$ spinel structure (JCPDS card 22-1086; space group $Fd\bar{3}m$).[50,51] There is not any evidence for the presence of any impurities can be marked in the XRD pattern of the $CoFe_2O_4$ product. The average crystallite size of $CoFe_2O_4$ nanoparticles (S46_600) was determined using the Debye–Scherrer formula (1) and estimated to be *ca.* 21.6 nm. Moreover, calcination of the carbonate composite samples (S46) at 400 and 500 °C for 2 h, generated pure $CoFe_2O_4$ products as well: S46_400, and S46_500, respectively (Fig. 1(b) and (c)), with different crystallite sizes; 9.5 and 15.2 nm, respectively, estimated from the XRD reflections using the Debye–Scherrer formula (1). On the other hand, calcination of the other carbonate composite samples produced impure products, as shown in Fig. 7(a)–(f).

Moreover, morphology and microstructure of the as-prepared $CoFe_2O_4$ product (S46_600) were examined using the FE-SEM and TEM. It is obvious that the spherical shape

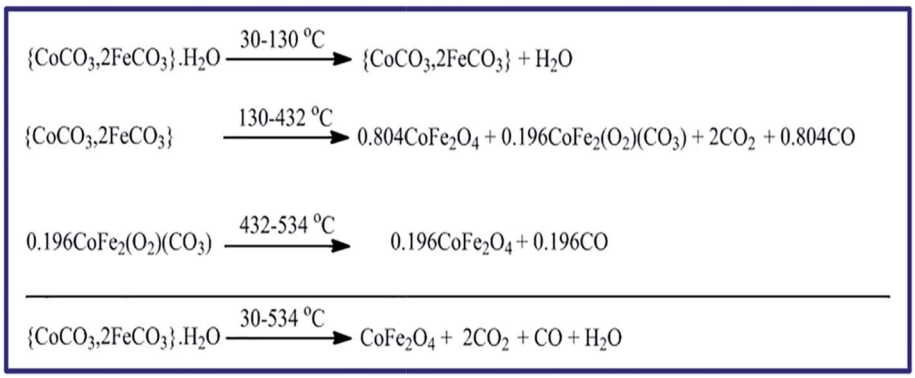

Scheme 3 Proposed thermal decomposition mechanism of $CoCO_3/FeCO_3$ nanocomposite precursor in N_2 gas atmosphere.

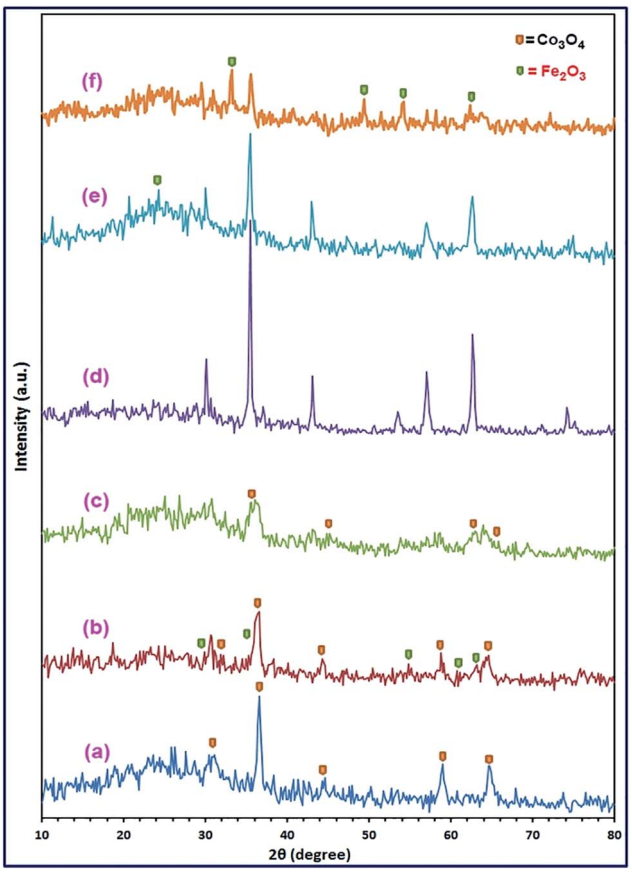

Fig. 7 XRD patterns of the calcination products; S19_600 (a), S37_600 (b), S46_600 (c), S11_600 (d), S37_600 (e), and S91_600 (f), of the respective $CoCO_3/FeCO_3$ composites at 600 °C for 2 h.

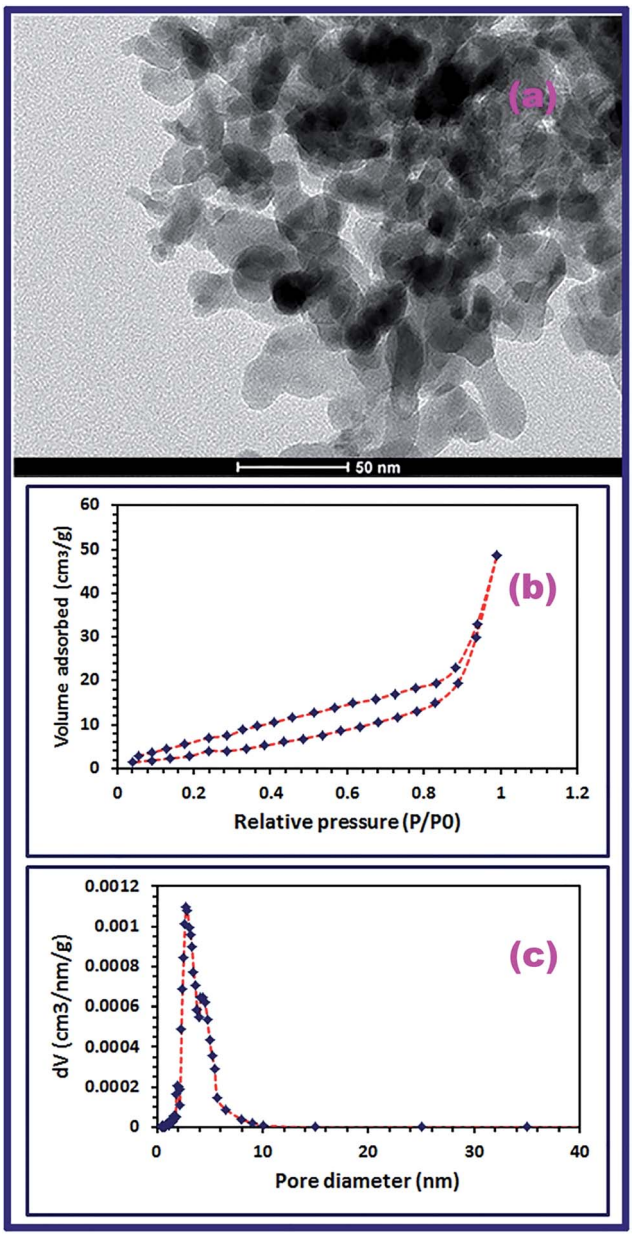

Fig. 8 TEM image of the $CoFe_2O_4$ product (a), N_2-adsorption–desorption isotherm (BET) (b), and BJH pore size distribution (c).

morphology of $CoCO_3/FeCO_3$ composite remained on calcination because the produced $CoFe_2O_4$ product is composed of uniform microspheres with average diameters of 4.19 and 1.7 μm, as shown in low magnification FE-SEM image, Fig. 4(c). Additionally, close inspection of the microspheres shown in the high magnification FE-SEM image (Fig. 4(d)) exhibited the porous nature characteristics of the $CoFe_2O_4$ product which indicate the hierarchical hollow structures of the microspheres. It is worthy to mention that the porous nature of the $CoFe_2O_4$ product may be due to: (i) the CO_2 and CO release during the calcination process of the carbonate precursor; and (ii) the presence of voids in the carbonate composite structure (Fig. 4(e) and (f)). Plus, the TEM micrograph (Fig. 8(a)) of the product shows that $CoFe_2O_4$ nanoparticles exist as dispersed and agglomerates of cube-like, square-like, and irregular particles with estimated average particle size of 22 nm which is in good agreement with the XRD data.

To further elucidate the chemical structure of the $CoFe_2O_4$ nanostructure (S46_600), FT-IR spectrum was carried out for the spinel product in the range of 4000–400 cm^{-1}, as displayed in Fig. 5(b). Fig. 5(b) reveals two intrinsic stretching vibrational absorption peaks confirming the spinel structure and purity of the as-prepared $CoFe_2O_4$ nanostructure. The first peak appeared at *ca.* 563 cm^{-1} may be assigned to the stretching vibrations of Co^{2+}–O and Fe^{3+}–O at the tetrahedral sites of the spinel structure. The second peak appeared at 406 cm^{-1} corresponds to the stretching vibrations of Fe^{3+}–O at the octahedral sites of the spinel structure. The gained results are compatible with the published data.[52–54] Additionally, Fig. 5(b) displays stretching and bending vibrations of the adsorbed water molecules, on the surfaces of the $CoFe_2O_4$ product (S46_600) nanoparticles, at 1610 and 3358 cm^{-1}, respectively, and this is in accordance with the reported results.[39,48,49] The BET surface area and porosity of the $CoFe_2O_4$ structure were examined using the N_2 adsorption–desorption isotherm analysis, as displayed in Fig. 8(b). Fig. 8(b) exhibits a hysteresis phenomenon similar to the IUPAC type-IV isotherm indicating

the presence of mesoporosity (*i.e.* pore size is in the range of 2–50 nm) in the involved in the structure of the product.[55] The BET surface area of the $CoFe_2O_4$ product was determined to be 31.2 $m^2\ g^{-1}$ and the Barrett–Joyner–Halenda (BJH) pore volume was evaluated to be 0.084 $cm^3\ g^{-1}$. The pore size distribution curve (Fig. 8(c)) shows that most parts of the product pore volume are filled by two groups of pores; one with 4.4 nm diameter and the other one with 2.7 nm diameter.

For additional identification of the product (S46_600), its point of zero charge (pH_{pzc}) and isoelectric point (IEP) were determined. The pH_{pzc} value was estimated using the pH drift method.[56] Thus, 0.01 M NaCl solution, different initial pHs (2–10; adjusted with 0.1 M HCl and NaOH solutions), and 0.05 g $CoFe_2O_4$ were employed. The as-prepared $CoFe_2O_4$ nanostructures (0.05 g) were suspended in each 25 mL of NaCl solution of a pre-adjusted pH, and allowed to stir at 25 °C for 48 h. Afterward, the final pH (pH_{final}) of the supernatant was measured after the oxide suspension separation. The $pH_{initial}$–pH_{final} curve was drawn using the measured $pH_{initial}$ and pH_{final} values; and from the intersection between this curve and the $pH_{initial} = pH_{final}$ line, the pH_{pzc} of the as-prepared $CoFe_2O_4$ nanoparticles could be estimated, as shown in Fig. 9(a). The pH_{pzc} of the $CoFe_2O_4$ nanostructure was estimated to be *ca.* 7.2 which was compatible with published values.[6,57] Additionally, the isoelectric point (IEP) of the as-prepared $CoFe_2O_4$ nanoparticles was determined using a zeta-potential analyzer at 25 °C. In this procedure, zeta potentials of $CoFe_2O_4$ suspensions in a series of 0.01 M NaCl solutions with various pH values (2–10) were measured. The zeta potential–$pH_{initial}$ curve was drawn as displayed in Fig. 9(b). And from this curve, the isoelectric point (IEP) of the as-prepared $CoFe_2O_4$ nanoparticles was evaluated to be *ca.* 7.5 which was in good agreement with the published data.[19,58]

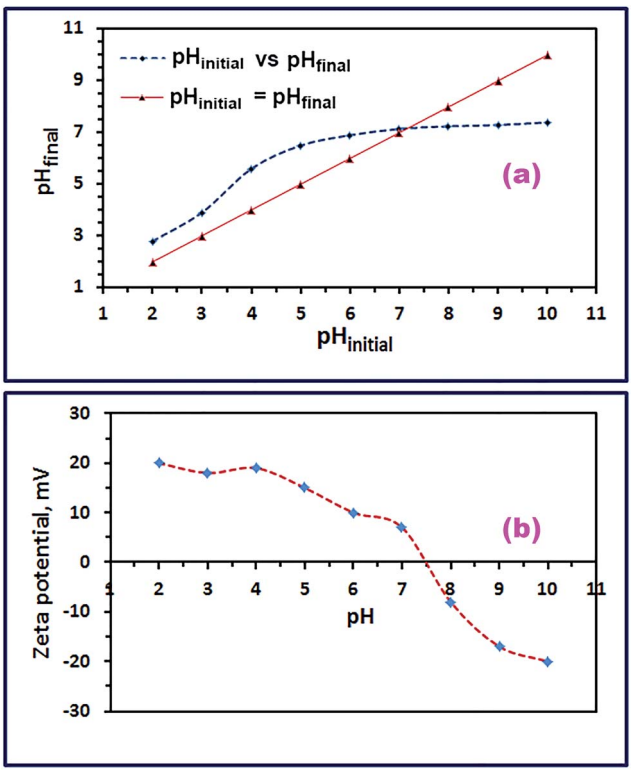

Fig. 9 $pH_{initial}$ *versus* pH_{final} graph for pH_{pzc} calculation for $CoFe_2O_4$ product (a), and zeta potential *versus* pH graph for IEP estimation for $CoFe_2O_4$ product (b).

3.3. Adsorption properties of $CoFe_2O_4$ nanoparticles

Adsorption of Reactive Red 195 dye (RR195) on the as-prepared $CoFe_2O_4$ adsorbent was explored. The FT-IR spectra can be utilized, as explained by Nassar *et al.* and others,[39,59] to support the adsorption process of a dye on an adsorbent, and this technique is used in the current investigation. Therefore, the FT-IR spectra of the bare adsorbent and the dye loaded adsorbent (*i.e.* after the adsorption process) were collected and presented in Fig. 5(b) and (c). Fig. 5(b) and (c) exhibits that there is a significant difference between the spectra of the bare and the RR195 dye loaded adsorbent. The vibrational absorptions appeared at 563 and 406 cm^{-1} for the ferrite spinel product (Fig. 5(b)) were shifted to 402 and 553 cm^{-1}, respectively, (after RR195 dye adsorption), as displayed in Fig. 5(c), and the last peak became broader. Plus, some new vibrational absorption peaks: 1028, 1181, 1364, 1414, and 1526 cm^{-1}, have been appeared attributing to the adsorbed RR195 dye molecules on the $CoFe_2O_4$ adsorbent, as depicted in Fig. 5(c).

3.3.1. Influence of pH. Due to the significant influence on the electrostatic interaction between the adsorbate molecules and the adsorbent nanoparticles, initial pH of the adsorption media has a crucial role in the adsorption process. For that reason, initial pH of the dye solution was investigated in the range of 1–10 to explore its effect on the adsorption process under the experimental conditions: 25 mL of RR195 dye with initial concentration (C_0) of 30 mg L^{-1}, 0.05 g of $CoFe_2O_4$ adsorbent, 25 °C, and for 24 h. The results are displayed in Fig. 10(a). The data revealed that higher adsorption capacity values were obtained at lower pHs (1–3), and the maximum adsorption capacity was attained at pH 2. Based on the point of zero charge value (7.2) and the isoelectric point (7.5), this may be due to the high electrostatic attraction between the positively charged $CoFe_2O_4$ nanoparticles and the negatively charged dye molecules at $pH < pH_{pzc}$. At pH values greater than 3, the RR195 dye adsorbed quantity decreases, and this may be attributed to the decrease in the number of the negatively charged sites of the adsorbent with increasing the pH. Similar behavior has been also noticed for adsorption of Congo red and RR195 dyes on different adsorbents.[19,25]

3.3.2. Influence of ionic strength. Dying containing industries usually exploit sodium chloride or other inorganic salts as stimulators during the dying process; and consequently, inorganic ions are included in the wastewaters discharged from this kind of industry. Accordingly, studying the effect of the presence of NaCl or KCl on the adsorption efficiency is an essential factor. The influence of the presence of KCl in the concentration range of 0.027–0.295 mol L^{-1} on the adsorption process of interest under the experimental conditions: 25 mL of RR195 dye with initial concentration (C_0) of 30 mg L^{-1}, 0.05 g of $CoFe_2O_4$ adsorbent, pH 2, 25 °C, and for 20 min (equilibration

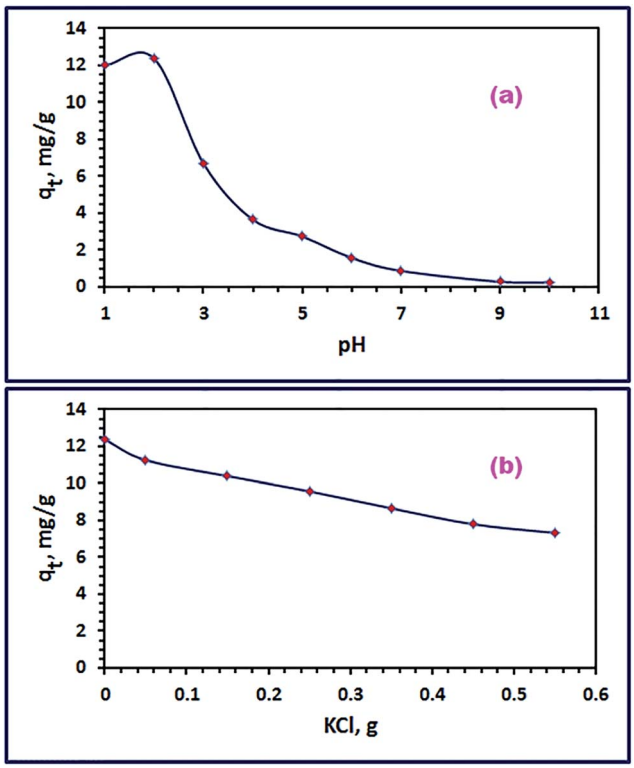

Fig. 10 Effect of pH (a), and ionic strength (b) on RR195 dye adsorption on $CoFe_2O_4$ adsorbent.

time as will be mentioned later), and the results are displayed in Fig. 10(b). It was indicated from Fig. 10(b) that the dye removal efficiency reduced (*i.e.* adsorption capacity of the nano-adsorbent) as the concentration of KCl enhanced. This behavior can be returned to the competition between the RR195 dye molecules and Cl^- anions for the active sites of the adsorbent, as reported by some research groups.[25,60]

3.3.3. Adsorption kinetics. To determine the equilibration time for the adsorption of RR195 dye on the as-prepared adsorbent ($CoFe_2O_4$), the influence of contact time on the dye removal efficiency was investigated in the range of 5–70 min under the experimental conditions: 25 mL of RR195 dye, initial dye concentration of 30 mg L^{-1}, 0.05 g of $CoFe_2O_4$ adsorbent, pH 2, and at 25 °C. The results are depicted in Fig. 11(a). The results reveal that the adsorption process is relatively fast which results in a short equilibration time (20 min); and as, the time elapses the removal efficiency reaches a constant value and the graph seems flattened.

Furthermore, to gain deep information about the kinetic order and mechanism of the adsorption process of the RR195 dye on the $CoFe_2O_4$ adsorbent, three kinetic models have been applied to examine the experimental adsorption data. The adopted kinetic models in the current study are pseudo-first order,[61] pseudo-second order,[62] and intra-particle diffusion model.[63] The linearized forms of the applied kinetic models can be written as given in eqn (6)–(8), respectively.

$$\log(q_e - q_t) = \log q_e - \frac{k_1}{2.303} t \quad (6)$$

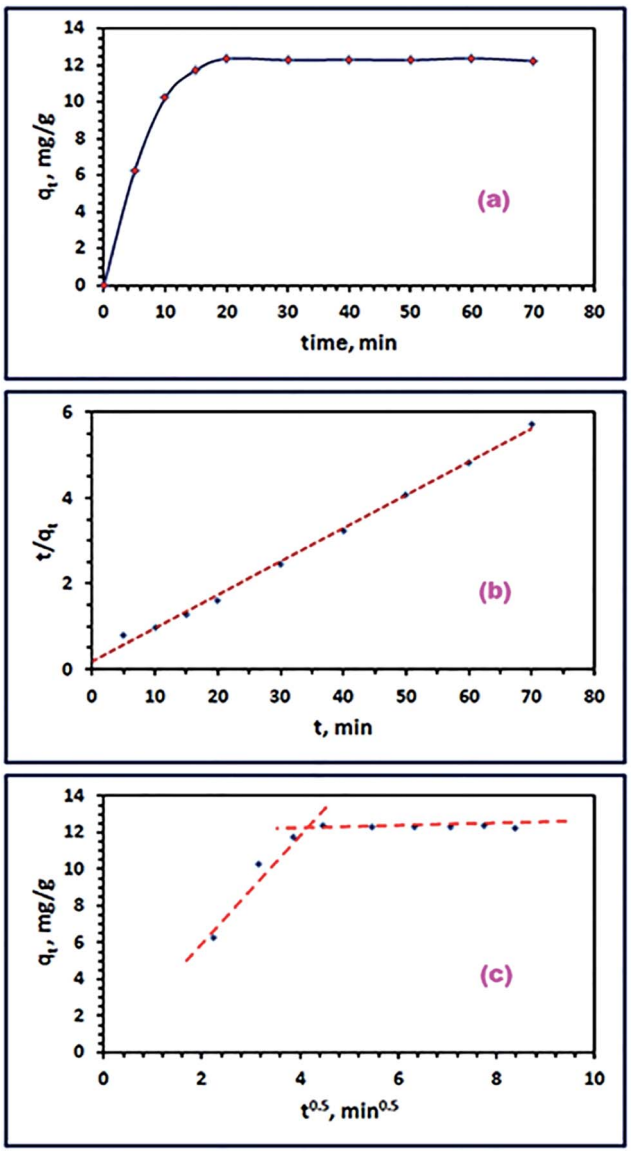

Fig. 11 Effect of time (a), pseudo-second-order (b), and Weber–Morris model (c) for the RR195 dye adsorption on $CoFe_2O_4$ adsorbent.

$$\frac{t}{q_t} = \frac{1}{k_2 q_e^2} + \frac{t}{q_e} \quad (7)$$

$$q_t = k_i t^{0.5} + C \quad (8)$$

where, t (min), q_t (mg g^{-1}), q_e (mg g^{-1}), k_1 (min^{-1}), k_2 (g mg^{-1} min^{-1}), k_i (mg (g $min^{1/2})^{-1}$), and C (mg g^{-1}) are the time of adsorption process, adsorption capacity of the $CoFe_2O_4$ adsorbent at time t, equilibrium adsorption capacity of $CoFe_2O_4$ adsorbent at the equilibration time, adsorption rate constant of pseudo-first-order model, adsorption rate constant of pseudo-second-order model, adsorption rate constant of the intra-particle diffusion model, and the intercept of the plot of eqn (8) indicating the boundary layer thickness, respectively. The calculated kinetic parameters for the adsorption process obtained from the aforementioned models are listed in Table 1.

Table 1 Kinetic parameters for the adsorption of RR195 dye on $CoFe_2O_4$ adsorbent

Kinetics models	Parameters	Value
Pseudo-first order	k_1 (min^{-1})	0.063
	$q_{e(cal)}$ (mg g^{-1})	2.18
	r_1^2	0.45
	$q_{e(exp)}$ (mg g^{-1})	12.4
Pseudo-second order	k_2 [g (mg min)$^{-1}$]	0.013
	$q_{e(cal)}$ (mg g^{-1})	12.9
	r_2^2	0.997
	$q_{e,exp}$ (mg g^{-1})	12.4

The pseudo-first-order rate constant was obtained from the slope of plotting $\log(q_e - q_t)$ *versus* t (results are not shown), as clear from eqn (6). The adsorption rate constant of the pseudo-second-order equation can be estimated from the intercept and slope of the graph resulted from the plot of t/q_t against t (Fig. 11(b)). It is clear from Table 1 that the adsorption of RR195 dye on $CoFe_2O_4$ adsorbent can be well described using the pseudo-second-order model because the correlation coefficient (r^2) value of this model is closer to unity (0.997) while that of the pseudo-first-order rate model is equal to 0.45. Moreover, the estimated adsorption capacity ($q_{e(cal)}$) value is in good agreement with the experimentally obtained one ($q_{e(exp)}$). Accordingly, the rate constant of the pseudo-second-order rate model could be employed to determine the initial sorption rate (h) using eqn (9) and presented in Table 1.[64]

$$h = k_2 q_e^2 \quad (9)$$

To determine whether the adsorption of RR195 dye on the as-prepared nano-adsorbent is controlled by a pure diffusion mechanism or not, the Weber and Morris model (eqn (8)) has been applied. Plotting of q_t *versus* $t^{0.5}$ values gives a multi-linear curve and does not go through the origin, as shown in Fig. 11(c). This behavior means that the rate determining step of the adsorption process – under study – is not only controlled by the intra-particle diffusion mechanism but controlled also by other mechanisms such as film diffusion and bulk diffusion along with the intra-particle diffusion mechanism.[65]

3.3.4. Influence of initial RR195 dye concentration and isothermal study. To gain more information about the adsorption mechanism of RR195 dye on $CoFe_2O_4$ adsorbent, different adsorption isotherms have been adopted. Therefore, the effect of initial concentration of RR195 dye on its adsorption on the as-prepared nano-adsorbent was examined under experimental conditions: 25 mL of RR195 dye, 10–80 mg L^{-1} initial dye concentration, 0.05 g of $CoFe_2O_4$ adsorbent, pH 2, and at 25 °C. The results are depicted in Fig. 12(a). Fig. 12(a) revealed that the adsorption capacity of the adsorbent enhanced with increasing the initial dye concentration till it reached maximum ($q_{e(exp)}$ = 18.2 mg g^{-1}) at initial dye concentration of 50 mg L^{-1}. At initial dye concentrations greater than 50 mg L^{-1}, the adsorption capacity of the adsorbent remained almost constant. This constancy might be returned to the attained saturation of the surface sites available for adsorption on the nano-adsorbent at high initial dye concentrations.

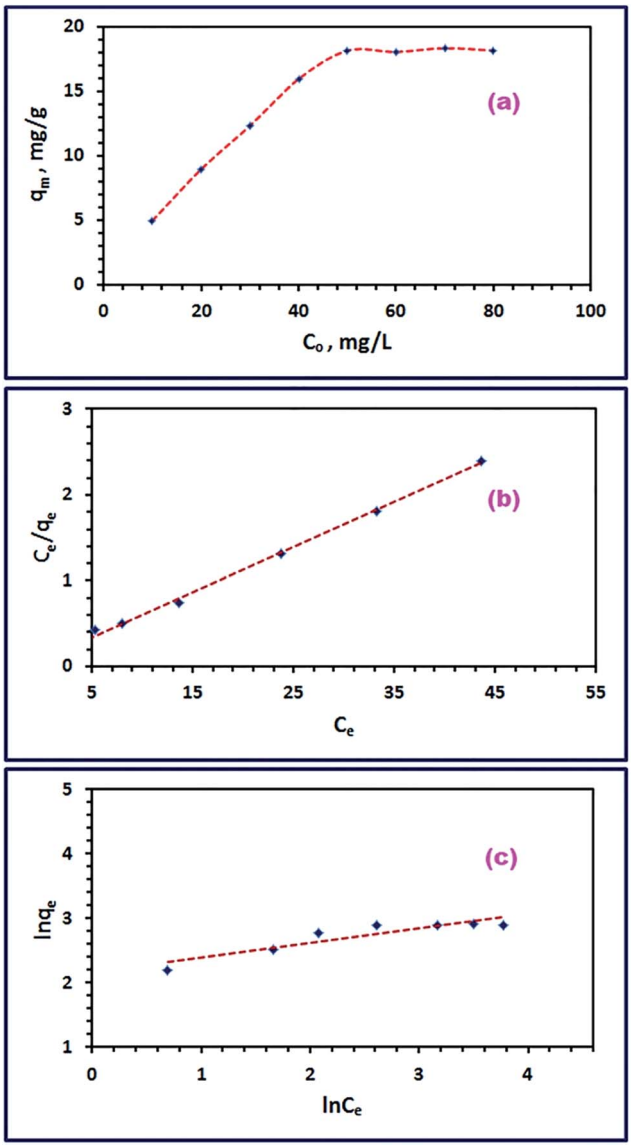

Fig. 12 Effect of initial RR195 dye concentration (a), Langmuir isotherm model (b), and Freundlich isotherm model (c) for RR195 dye adsorption on $CoFe_2O_4$ adsorbent.

On the other hand, the obtained adsorption data have been tested using two well-known adsorption isotherms: Langmuir and Freundlich isotherm models, to understand the adsorption mechanism of the dye of interest. Where, the Langmuir model supposes that there is no interaction between the adsorbed molecules on an adsorbent homogenous surfaces, and the Freundlich model proposes that the adsorption occurs on an adsorbent heterogeneous surfaces. The mathematical expressions for the Langmuir and Freundlich isotherm models can be written as given in eqn (10) and (11), respectively.

$$\frac{C_e}{q_e} = \frac{1}{K_L q_m} + \frac{C_e}{q_m} \quad (10)$$

$$\ln q_e = \ln K_F + \frac{1}{n}\ln C_e \quad (11)$$

where, C_e (mg L^{-1}), q_e (mg g^{-1}), K_L (L mg^{-1}), q_m (mg g^{-1}), K_F [(mg g^{-1})(L mg^{-1})$^{1/n}$], and n are the equilibrium concentration of the RR195 dye, the adsorbed quantity of the RR195 dye at equilibrium, Langmuir constant, maximum adsorption capacity of the nano-adsorbent for RR195 dye, Freundlich constant, and constant (indicating the adsorption intensity in case of Freundlich isotherm model), respectively. According to eqn (10) (Langmuir isotherm model), q_m and K_L parameters can be estimated from the slope and intercept of the plot of C_e/q_e against C_e, as depicted in Fig. 12(b). Also, based on eqn (11) (Freundlich isotherm model), K_F and n constants can be calculated from the slope and intercept of the plot of ln q_e against ln C_e, as displayed in Fig. 12(c). Despite, it is well-known that the q_m value can be estimated using the Langmuir isotherm equation; as aforementioned, q_m can also be determined using the Freundlich isotherm model by utilizing eqn (12) according to Halsey.[66]

$$K_F = \frac{q_m}{C_0^{1/n}} \quad (12)$$

The calculated constants for both isotherm models are tabulated in Table 2. Inspection of the data presented in Table 2 (especially the correlation coefficient values (r^2)) exhibits that the experimental adsorption data can be well described using the Langmuir isotherm model. Furthermore, the calculated maximum adsorption capacity ($q_{m(cal)}$, 18.9 mg g^{-1}) based on the Langmuir isotherm model is in good agreement with the experimentally obtained one ($q_{e(exp)}$, 18.2 mg g^{-1}). These results indicate the homogenous nature of the as-prepared adsorbent, and the adsorption of RR195 dye on the $CoFe_2O_4$ adsorbent is monolayer coverage because the experimental data fit well the Langmuir isotherm model.

Additionally, the adsorption efficiency of RR195 dye on $CoFe_2O_4$ adsorbent was examined using the dimensionless constant, R_L, expressed as follows:

$$R_L = \frac{1}{1 + K_L C_0} \quad (13)$$

where, C_0 (mg L^{-1}) and K_L (L mg^{-1}) are the initial RR195 dye concentration and Langmuir constant, respectively. The calculated value of R_L constant indicates whether the adsorption of RR195 dye on $CoFe_2O_4$ adsorbent is favorable ($0 < R_L < 1$), linear ($R_L = 1$), irreversible ($R_L = 0$), or unfavorable ($R_L > 1$).[67] In the present study, the R_L values were found to be in the range of 0.121–0.017, for the initial concentration range of 10–80 mg L^{-1}, respectively, implying that the adsorption of RR195 dye on $CoFe_2O_4$ adsorbent is a favorable process.

Table 2 Langmuir and Freundlich isotherm constants for the adsorption of RR195 dye on $CoFe_2O_4$ adsorbent

Adsorption isotherm	Parameters	Value
Langmuir	K_L (L mg^{-1})	0.727
	$q_{m(cal)}$ (mg g^{-1})	18.9
	r_1^2	0.997
	R_L	0.121 to 0.017
	$q_{e(exp)}$ (mg g^{-1})	18.2
Freundlich	K_F [(mg g^{-1})(L mg^{-1})$^{1/n}$]	8.64
	$q_{m(cal)}$ (mg g^{-1})	21.2
	r_2^2	0.840
	n	4.37
	$q_{e(exp)}$ (mg g^{-1})	18.2

3.3.5. Influence of temperature and adsorption thermodynamic study. Under the optimized adsorption conditions (25 mL of RR195 dye, 50 mg L^{-1} initial dye concentration, 0.05 g of $CoFe_2O_4$ adsorbent, and pH 2), some adsorption experiments were performed at different temperatures (298, 308, 318, and 328 K) to explore the influence of temperature on the adsorption process. Consequently, some thermodynamic constants such as a change in enthalpy (ΔH^0), change in the entropy (ΔS^0), and change in free energy (ΔG^0) were calculated utilizing the following equations:[25,68]

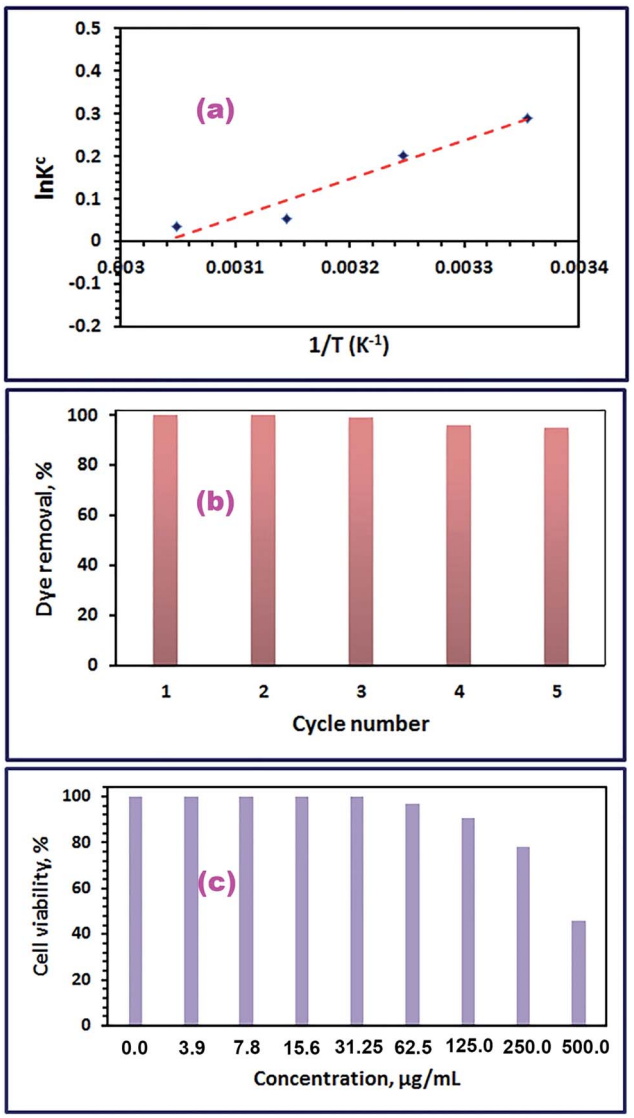

Fig. 13 Plot of ln K_c *versus* 1/T (a), effect of regeneration cycle on the efficiency of $CoFe_2O_4$ adsorbent for RR195 dye removal (b), and cell viability assessment of $CoFe_2O_4$ adsorbent at pH 2 (c).

Table 3 Thermodynamic constants for the adsorption of RR195 dye on $CoFe_2O_4$ adsorbent

Temperature (K)	K_c	ΔG^0 (kJ mol^{-1})	ΔS^0 (J mol^{-1} K^{-1})	ΔH^0 (kJ mol^{-1})
298	1.34	−0.711	−0.023	−7.55
308	1.22	−0.481		
318	1.05	−0.252		
328	1.03	−0.022		

$$\ln K_c = \frac{\Delta S^0}{R} - \frac{\Delta H^0}{RT} \quad (14)$$

$$\Delta G^0 = \Delta H^0 - T\Delta S^0 \quad (15)$$

where, K_c (L g^{-1}), R (kJ mol^{-1} K^{-1}), and T (K) are the thermodynamic equilibrium constant which is equal to q_e/C_e (*i.e.* $K_c = q_e/C_e$), universal gas constant (8.314×10^{-3} kJ mol^{-1} K^{-1}), and absolute temperature of the solution, respectively. The value of K_c was determined at different temperatures, and plotting of $\ln K_c$ *versus* $1/T$ values resulted in a straight line, as displayed in Fig. 13(a). The values of ΔH^0 and ΔS^0 were calculated from the slope and intercept of the obtained line (Fig. 13(a)). By knowing ΔH^0 and ΔS^0 values and feeding them into eqn (15), ΔG^0 values can be estimated. The calculated thermodynamic constants are presented in Table 3. The obtained ΔG^0 negative values indicate feasibility and spontaneity of the adsorption of RR195 dye on $CoFe_2O_4$ nano-adsorbent. Besides, the negative values of ΔH^0 (−7.55 kJ mol^{-1}) imply the exothermic nature of the adsorption process. As the ΔH^0 values are smaller than 40 kJ mol^{-1}, and the ΔG^0 values (from −0.71 to −0.022 kJ mol^{-1}) are in the range from −20 to 0 kJ mol^{-1}, it can be concluded that the adsorption of RR195 dye on the as-synthesized $CoFe_2O_4$ nanoparticles is a physisorption process.

3.3.6. The reusability of $CoFe_2O_4$ adsorbent and effect of surface area on the adsorption process. The adsorption of the RR195 dye on the nano-sized $CoFe_2O_4$ adsorbent can be influenced by tuning the surface area of $CoFe_2O_4$ adsorbent. The surface area of the adsorbent can be controlled by calcination of the carbonate composite precursor at different temperatures: 400, 500, and 600 °C, to generate $CoFe_2O_4$ nanoparticles: S46_400, S46_500, and S46_600, respectively, with different crystallite sizes. The BET surface area, crystallite size, total pore volume, and BJH pore size of the $CoFe_2O_4$ products: S46_400, S46_500, and S46_600, were estimated, and the results were listed in Table 4. It is obvious that the BET surface area of $CoFe_2O_4$ nanoparticles enhances in the following order: S46_400 > S46_500 > S46_600, which is the same order of the BJH pore volumes for the $CoFe_2O_4$ products. This order may be due to that the smaller the crystallite size and the greater the pore volume, the larger the surface area of the product. The effects of surface areas of the $CoFe_2O_4$ products, calcined at temperatures, on the adsorption of the RR195 dye were studied under the obtained optimum conditions. Then, the maximum adsorption capacities were determined and presented in Table 4. The results showed that the $CoFe_2O_4$ product (S46_400) has the highest maximum adsorption capacity (91.2 mg g^{-1}), and the order of the maximum adsorption capacities is S46_400 > S46_500 > S46_600 which is compatible with the aforementioned order of the surface area of the products. Additionally, the results may be interpreted on the basis that samples with higher surface area provide more active sites for adsorption of the dye molecules; and consequently, this yields higher maximum adsorption capacities.[25]

Furthermore, the regeneration of the $CoFe_2O_4$ adsorbent and its reusability for the adsorption of RR195 dye have been investigated because they are essential from the overall cost point of view for the application purposes. Hence, the adsorption of RR195 dye on the as-synthesized $CoFe_2O_4$ adsorbent (S46_400) was carried under the obtained optimum adsorption conditions; then, the dye-loaded $CoFe_2O_4$ adsorbent was regenerated by either extraction of the adsorbed dye using methanol followed by washing with methanol and water then drying for 6 h at *ca.* 60 °C; or combustion of the dye-loaded $CoFe_2O_4$ adsorbent at *ca.* 450 °C for 30 min. The recycling procedure was repeated five times, and the results were displayed in Fig. 13(b). The results reveal that, after five cycles of reuse, the as-synthesized $CoFe_2O_4$ adsorbent (S46_400) still has good reproducibility and adsorption efficiency (*ca.* 95%). Therefore, the collected results support the long term use of the $CoFe_2O_4$ adsorbent, and also reflect that the as-synthesized spinel $CoFe_2O_4$ can be suggested as a good candidate for the removal of RR195 dye from aqueous solutions.

3.3.7. Comparison of $CoFe_2O_4$ adsorbent performance with other adsorbents. The maximum adsorption capacities (q_m) of various adsorbents including the as-synthesized $CoFe_2O_4$ adsorbent for the removal of RR195 dye are tabulated in Table 5. The results show that the as-prepared $CoFe_2O_4$ adsorbent has a relatively high value of q_m compared to the q_m values of the other adsorbents listed in Table 5. While some other adsorbents have higher q_m values toward RR195 dye, the as-synthesized $CoFe_2O_4$ adsorbent has several characteristics: its five-cycle reusability, 100% desorption ratio, and the overall cost of this adsorbent, which make this adsorbent a good candidate for the removal of RR195 dye from aqueous solutions.

Table 4 BET surface area, crystallite size, pore size, and pore volume of $CoFe_2O_4$ samples and their adsorption capacities for RR195 dye

Adsorbent sample	Crystallite size, nm	BET surface area, m^2 g^{-1}	BJH pore diameter (nm)	BJH pore volume (cm^3 g^{-1})	Removal adsorption capacity (mg g^{-1})
S46_400	9.5	120.3	2.6	0.21	91.2
S46_500	15.2	65.7	3.1	0.14	39.2
S46_600	21.6	31.2	4.4	0.084	18.9

Table 5 Comparison of adsorption capacities with different adsorbents including $CoFe_2O_4$ adsorbent (S46_400) toward RR195 dye removal

Adsorbent material	Adsorption capacities, q_m, mg g^{-1}	Ref.
Cone biomass	7.38	69
α-Fe_2O_3	20.5	25
Modified palygorskite with 3-aminopropyl triethoxysilane	34.24	70
Dehydrated beet pulp carbon	58.0	71
TiO_2	87	72
$CoFe_2O_4$	91.7	Present study
Wheat bran	119.1	73

In addition, the as-prepared $CoFe_2O_4$ adsorbent showed high chemical stability because the analyzed concentrations of the cobalt and iron ions released from the adsorbent, at pH 2, were found to be *ca.* 0.020 and 0.001 mg L^{-1}, respectively, after 24 h contact time. And the leached cobalt and iron ions concentrations (at pH 2, and after 48 h contact time) were estimated to be *ca.* 0.047 and 0.002 mg L^{-1}, respectively. Therefore, low concentrations of the released ions from the as-prepared adsorbent will not result in environmental metal pollution. Moreover, the cytotoxicity of the $CoFe_2O_4$ nanoparticles against normal human fibroblast cell line was evaluated using MTT assay. The cell viability results after cell exposure to the $CoFe_2O_4$ nanoparticles were displayed in Fig. 13(c). The results exhibited that the viability of the MRC-5 cells was $CoFe_2O_4$ concentration dependent, and the cells were viable after exposure to $CoFe_2O_4$ with a concentration of 469 μg mL^{-1} (*i.e.* CC_{50} = 469 μg mL^{-1}). Therefore, we may deduce that the as-prepared $CoFe_2O_4$ adsorbent has relatively high chemical stability and low cytotoxicity since the concentrations of the leached cobalt and iron ions are low.

4. Conclusions

In this work, pure spinel $CoFe_2O_4$ nanostructure was successfully synthesized *via* a template-free hydrothermal and post thermal conversion route. Therefore, pure $CoCO_3/FeCO_3$ nanocomposite precursors were hydrothermally prepared in high yield by the hydrothermal reaction of Co^{2+}, Fe^{2+}, ascorbic acid, and ammonium carbonate in the presence of sulfate counter ion. The Co^{2+} : Fe^{2+} molar ratio has a remarkable effect on the hydrothermal reaction. Thermal decomposition of the pure $CoCO_3/FeCO_3$ nanocomposite precursor synthesized using $0.4Co^{2+}$: $0.6Fe^{2+}$ molar ratio is the only precursor that produced pure spinel $CoFe_2O_4$ nanostructure. The as-synthesized $CoFe_2O_4$ nano-adsorbent revealed good adsorption capacity (91.7 mg g^{-1}) for the removal of Reactive Red 195 (RR195) dye. The adsorption results could be described well by the pseudo-second-order kinetics. The adsorption isothermal results revealed the monolayer coverage of the RR195 dye molecules on $CoFe_2O_4$ nano-adsorbent. Besides, the thermodynamic results exhibited that the adsorption of RR195 dye on the $CoFe_2O_4$ nano-adsorbent is spontaneous, exothermic, and physisorptive process. In addition, the as-prepared $CoFe_2O_4$ product can be considered as a promising adsorbent for the removal of RR195 dye from aqueous solutions.

Acknowledgements

This research was financially supported by Benha University. The first author (Mostafa Y Nassar) is grateful to Professor Ibrahim S. Ahmed, Chem. Dept, Faculty of Science, Benha University for his support.

References

1 H. Li, Z. Lu, G. Cheng, K. Rong, F. Chen and R. Chen, HEPES-involved hydrothermal synthesis of Fe_3O_4 nanoparticles and their biological application, *RSC Adv.*, 2015, **5**, 5059–5067.
2 W. Wang, T. Jiao, Q. Zhang, X. Luo, J. Hu, Y. Chen, Q. Peng, X. Yan and B. Li, Hydrothermal synthesis of hierarchical core–shell manganese oxide nanocomposites as efficient dye adsorbents for wastewater treatment, *RSC Adv.*, 2015, **5**, 56279–56285.
3 T. Jiao, Y. Liu, Y. Wu, Q. Zhang, X. Yan, F. Gao, A. J. P. Bauer, J. Liu, T. Zeng and B. Li, Facile and Scalable Preparation of Graphene Oxide-Based Magnetic Hybrids for Fast and Highly Efficient Removal of Organic Dyes, *Sci. Rep.*, 2015, **5**, 12451.
4 H. Emadi and A. N. Kharat, Synthesis and characterization of ultrafine and mesoporous structure of cobalt ferrite, *J. Ind. Eng. Chem.*, 2015, **21**, 951–956.
5 M. Gu, B. Yue, R. Bao and H. He, Template synthesis of magnetic one-dimensional nanostructured spinel MFe_2O_4 (M = Ni, Mg, Co), *Mater. Res. Bull.*, 2009, **44**, 1422–1427.
6 D. H. K. Reddy and Y.-S. Yun, Spinel ferrite magnetic adsorbents: alternative future materials for water purification?, *Coord. Chem. Rev.*, 2016, **315**, 90–111.
7 Y. Choi, B. S. Seong and S. S. Kim, Characterization and structural analysis of nano-sized Ba–Zn ferrite powders prepared by using a self-propagating high-temperature synthesis reaction and mechanical milling, *Phys. B*, 2009, **404**, 689–691.
8 M. Chithra, C. N. Anumol, B. Sahu and S. C. Sahoo, Exchange spring like magnetic behavior in cobalt ferrite nanoparticles, *J. Magn. Magn. Mater.*, 2016, **401**, 1–8.
9 J. Zhou, J. Ma, C. Sun, L. Xie, Z. Zhao, H. Tian, Y. Wang, J. Tao and X. Zhu, Low-Temperature Synthesis of $NiFe_2O_4$ by a Hydrothermal Method, *J. Am. Ceram. Soc.*, 2005, **88**, 3535–3537.
10 Y. Wang, L. Li, J. Jiang, H. Liu, H. Qiu and F. Xu, Conductivity and magnetic properties of $Zn_{0.6}Cu_{0.4}Cr_{0.5}La_{0.04}Fe_{1.46}O_4$/PPy composites prepared by *in situ* inverse microemulsion polymerization, *React. Funct. Polym.*, 2008, **68**, 1587–1593.
11 S. Thakur, S. C. Katyal and M. Singh, Structural and magnetic properties of nano nickel–zinc ferrite synthesized by reverse micelle technique, *J. Magn. Magn. Mater.*, 2009, **321**, 1–7.

12 J. Wang, T. Deng, Y. Lin, C. Yang and W. Zhan, Synthesis and characterization of $CoFe_2O_4$ magnetic particles prepared by co-precipitation method: effect of mixture procedures of initial solution, *J. Alloys Compd.*, 2008, **450**, 532–539.
13 P. E. Meskin, V. K. Ivanov, A. E. Barantchikov, B. R. Churagulov and Y. D. Tretyakov, Ultrasonically assisted hydrothermal synthesis of nanocrystalline ZrO_2, TiO_2, $NiFe_2O_4$ and $Ni_{0.5}Zn_{0.5}Fe_2O_4$ powders, *Ultrason. Sonochem.*, 2006, **13**, 47–53.
14 G. Wang, Y. Ma, X. Dong, Y. Tong, L. Zhang, J. Mu, Y. Bai, J. Hou, H. Che and X. Zhang, Facile synthesis and magnetorheological properties of superparamagnetic $CoFe_2O_4$/GO nanocomposites, *Appl. Surf. Sci.*, 2015, **357**, 2131–2135.
15 X. Guoxi and X. Yuebin, Effects on magnetic properties of different metal ions substitution cobalt ferrites synthesis by sol–gel auto-combustion route using used batteries, *Mater. Lett.*, 2016, **164**, 444–448.
16 J. Fu, J. Zhang, Y. Peng, J. Zhao, G. Tan, N. J. Mellors, E. Xie and W. Han, Unique magnetic properties and magnetization reversal process of $CoFe_2O_4$ nanotubes fabricated by electrospinning, *Nanoscale*, 2012, **4**, 3932–3936.
17 J. T. Korhonen, P. Hiekkataipale, J. Malm, M. Karppinen, O. Ikkala and R. H. A. Ras, Inorganic Hollow Nanotube Aerogels by Atomic Layer Deposition onto Native Nanocellulose Templates, *ACS Nano*, 2011, **5**, 1967–1974.
18 M. Houshiar, F. Zebhi, Z. J. Razi, A. Alidoust and Z. Askari, Synthesis of cobalt ferrite ($CoFe_2O_4$) nanoparticles using combustion, coprecipitation, and precipitation methods: a comparison study of size, structural, and magnetic properties, *J. Magn. Magn. Mater.*, 2014, **371**, 43–48.
19 S. Yavari, N. M. Mahmodi, P. Teymouri, B. Shahmoradi and A. Maleki, Cobalt ferrite nanoparticles: preparation, characterization and anionic dye removal capability, *J. Taiwan Inst. Chem. Eng.*, 2016, **59**, 320–329.
20 V. Pillai and D. O. Shah, Synthesis of high-coercivity cobalt ferrite particles using water-in-oil microemulsions, *J. Magn. Magn. Mater.*, 1996, **163**, 243–248.
21 M. Y. Nassar and I. S. Ahmed, Hydrothermal synthesis of cobalt carbonates using different counter ions: an efficient precursor to nano-sized cobalt oxide (Co_3O_4), *Polyhedron*, 2011, **30**, 2431–2437.
22 M. Y. Nassar, T. Y. Mohamed and I. S. Ahmed, One-pot solvothermal synthesis of novel cobalt salicylaldimine–urea complexes: a new approach to Co_3O_4 nanoparticles, *J. Mol. Struct.*, 2013, **1050**, 81–87.
23 M. Y. Nassar, Size-controlled synthesis of $CoCO_3$ and Co_3O_4 nanoparticles by free-surfactant hydrothermal method, *Mater. Lett.*, 2013, **94**, 112–115.
24 M. Y. Nassar and I. S. Ahmed, Template-free hydrothermal derived cobalt oxide nanopowders: synthesis, characterization, and removal of organic dyes, *Mater. Res. Bull.*, 2012, **47**, 2638–2645.
25 M. Y. Nassar, I. S. Ahmed, T. Y. Mohamed and M. Khatab, A controlled, template-free, and hydrothermal synthesis route to sphere-like [small alpha]-Fe_2O_3 nanostructures for textile dye removal, *RSC Adv.*, 2016, **6**, 20001–20013.
26 Z. Liu, X. Zhou, Y. Zhang, Q. Liu, Q. Liu, B. Li, G. Zhu, D. Li and X. Li, Fabrication of monodispersed, uniform rod-shaped $FeCO_3$/$CoCO_3$ microparticles using a facile solvothermal method and their excellent microwave absorbing properties, *J. Alloys Compd.*, 2016, **665**, 388–393.
27 T. A. Khan, S. Dahiya and I. Ali, Use of kaolinite as adsorbent: equilibrium, dynamics and thermodynamic studies on the adsorption of rhodamine B from aqueous solution, *Appl. Clay Sci.*, 2012, **69**, 58–66.
28 H. M. Aly, M. E. Moustafa, M. Y. Nassar and E. A. Abdelrahman, Synthesis and Characterization of Novel Cu (II) Complexes with 3-Substituted-4-Amino-5-Mercapto-1,2,4-Triazole Schiff Bases: A New Route to Cuo Nanoparticles, *J. Mol. Struct.*, 2015, **1086**, 223–231.
29 A. Nematollahzadeh, A. Shojaei and M. Karimi, Chemically modified organic/inorganic nanoporous composite particles for the adsorption of reactive black 5 from aqueous solution, *React. Funct. Polym.*, 2015, **86**, 7–15.
30 M. Y. Nassar, I. S. Ahmed and I. Samir, A novel synthetic route for magnesium aluminate ($MgAl_2O_4$) nanoparticles using sol–gel auto combustion method and their photocatalytic properties, *Spectrochim. Acta, Part A*, 2014, **131**, 329–334.
31 C. Yang, Y. Zhu, J. Wang, Z. Li, X. Su and C. Niu, Hydrothermal synthesis of TiO_2–WO_3–bentonite composites: conventional *versus* ultrasonic pretreatments and their adsorption of methylene blue, *Appl. Clay Sci.*, 2015, **105–106**, 243–251.
32 R. Bhattacharyya and S. K. Ray, Micro- and nano-sized bentonite filled composite superabsorbents of chitosan and acrylic copolymer for removal of synthetic dyes from water, *Appl. Clay Sci.*, 2014, **101**, 510–520.
33 C.-C. Lin, Y.-S. Lin and J.-M. Ho, Adsorption of Reactive Red 2 from aqueous solutions using Fe_3O_4 nanoparticles prepared by co-precipitation in a rotating packed bed, *J. Alloys Compd.*, 2016, **666**, 153–158.
34 A. R. Tehrani-Bagha, M. Gharagozlou and F. Emami, Catalytic wet peroxide oxidation of a reactive dye by magnetic copper ferrite nanoparticles, *J. Environ. Chem. Eng.*, 2016, **4**, 1530–1536.
35 A. Afkhami, S. Sayari, R. Moosavi and T. Madrakian, Magnetic nickel zinc ferrite nanocomposite as an efficient adsorbent for the removal of organic dyes from aqueous solutions, *J. Ind. Eng. Chem.*, 2015, **21**, 920–924.
36 W. Konicki, D. Sibera, E. Mijowska, Z. Lendzion-Bieluń and U. Narkiewicz, Equilibrium and kinetic studies on acid dye Acid Red 88 adsorption by magnetic $ZnFe_2O_4$ spinel ferrite nanoparticles, *J. Colloid Interface Sci.*, 2013, **398**, 152–160.
37 T. Mosmann, Rapid colorimetric assay for cellular growth and survival: application to proliferation and cytotoxicity assays, *J. Immunol. Methods*, 1983, **65**, 55–63.
38 S. M. Gomha, S. M. Riyadh, E. A. Mahmmoud and M. M. Elaasser, Synthesis and Anticancer Activities of Thiazoles, 1,3-Thiazines, and Thiazolidine Using Chitosan-Grafted-Poly(vinylpyridine) as Basic Catalyst, *Heterocycles*, 2015, **91**, 1227–1243.

39 M. Y. Nassar, M. M. Moustafa and M. M. Taha, A hydrothermal tuning of the morphology and particle size of hydrozincite nanoparticles using different counter ions to produce nano-sized ZnO as an efficient adsorbent for textile dye removal, *RSC Adv.*, 2016, **6**, 42180–42195.

40 H.-P. Cong and S.-H. Yu, Shape Control of Cobalt Carbonate Particles by a Hydrothermal Process in a Mixed Solvent: An Efficient Precursor to Nanoporous Cobalt Oxide Architectures and Their Sensing Property, *Cryst. Growth Des.*, 2009, **9**, 210–217.

41 M. Chirita and A. Ieta, $FeCO_3$ Microparticle Synthesis by Fe-EDTA Hydrothermal Decomposition, *Cryst. Growth Des.*, 2012, **12**, 883–886.

42 R. Jenkins and R. L. Snyder, *Introduction to X-ray powder diffractometry*, John Wiley & Sons, Inc., New York, 1996.

43 Y. Tang, T. Chen and S. Yu, Morphology controlled synthesis of monodispersed manganese sulfide nanocrystals and their primary application in supercapacitors with high performances, *Chem. Commun.*, 2015, **51**, 9018–9021.

44 Y. Tang, Y. Liu, S. Yu, W. Guo, S. Mu, H. Wang, Y. Zhao, L. Hou, Y. Fan and F. Gao, Template-free hydrothermal synthesis of nickel cobalt hydroxide nanoflowers with high performance for asymmetric supercapacitor, *Electrochim. Acta*, 2015, **161**, 279–289.

45 A. Askarinejad and A. Morsali, Synthesis of cadmium(II) hydroxide, cadmium(II) carbonate and cadmium(II) oxide nanoparticles; investigation of intermediate products, *Chem. Eng. J.*, 2009, **150**, 569–571.

46 X. W. Lou, D. Deng, J. Y. Lee and L. A. Archer, Thermal formation of mesoporous single-crystal Co_3O_4 nano-needles and their lithium storage properties, *J. Mater. Chem.*, 2008, **18**, 4397–4401.

47 S. Ashoka, P. Chithaiah and G. T. Chandrappa, Studies on the synthesis of $CdCO_3$ nanowires and porous CdO powder, *Mater. Lett.*, 2010, **64**, 173–176.

48 K. Nakamoto, *Infrared and Raman Spectra of Inorganic and Coordination Compounds, Applications in Coordination, Organometallic, and Bioinorganic Chemistry*, Wiley, 2009.

49 M. Y. Nassar, A. S. Attia, K. A. Alfallous and M. F. El-Shahat, Synthesis of two novel dinuclear molybdenum(0) complexes of quinoxaline-2,3-dione: new precursors for preparation of α-MoO_3 nanoplates, *Inorg. Chim. Acta*, 2013, **405**, 362–367.

50 M. Sundararajan, L. J. Kennedy, U. Aruldoss, S. K. Pasha, J. J. Vijaya and S. Dunn, Microwave combustion synthesis of zinc substituted nanocrystalline spinel cobalt ferrite: structural and magnetic studies, *Mater. Sci. Semicond. Process.*, 2015, **40**, 1–10.

51 E. Swatsitang, S. Phokha, S. Hunpratub, B. Usher, A. Bootchanont, S. Maensiri and P. Chindaprasirt, Characterization and magnetic properties of cobalt ferrite nanoparticles, *J. Alloys Compd.*, 2016, **664**, 792–797.

52 A. Goyal, S. Bansal, V. Kumar, J. Singh and S. Singhal, Mn substituted cobalt ferrites ($CoMn_xFe_{2-x}O_4$ ($x = 0.0$, 0.2, 0.4, 0.6, 0.8, 1.0)): as magnetically separable heterogeneous nanocatalyst for the reduction of nitrophenols, *Appl. Surf. Sci.*, 2015, **324**, 877–889.

53 M. Ben Ali, K. El Maalam, H. El Moussaoui, O. Mounkachi, M. Hamedoun, R. Masrour, E. K. Hlil and A. Benyoussef, Effect of zinc concentration on the structural and magnetic properties of mixed Co–Zn ferrites nanoparticles synthesized by sol/gel method, *J. Magn. Magn. Mater.*, 2016, **398**, 20–25.

54 E. Jaberolansar, P. Kameli, H. Ahmadvand and H. Salamati, Synthesis and characterization of PVP-coated ferrite nanoparticles, *J. Magn. Magn. Mater.*, 2016, **404**, 21–28.

55 M. Thommes, K. Kaneko, V. Neimark Alexander, P. Olivier James, F. Rodriguez-Reinoso, J. Rouquerol and S. W. Sing Kenneth, Physisorption of gases, with special reference to the evaluation of surface area and pore size distribution (IUPAC Technical Report), in *Pure and Applied Chemistry*, 2015, p. 1051.

56 M. Ahmaruzzaman and S. Laxmi Gayatri, Batch adsorption of 4-nitrophenol by acid activated jute stick char: equilibrium, kinetic and thermodynamic studies, *Chem. Eng. J.*, 2010, **158**, 173–180.

57 M. Kosmulski, pH-dependent surface charging and points of zero charge. IV Update and new approach, *J. Colloid Interface Sci.*, 2009, **337**, 439–448.

58 M. Kosmulski, The pH dependent surface charging and points of zero charge. VI Update, *J. Colloid Interface Sci.*, 2014, **426**, 209–212.

59 M. Y. Nassar, A. S. Amin, I. S. Ahmed and S. Abdallah, Sphere-like Mn_2O_3 nanoparticles: facile hydrothermal synthesis and adsorption properties, *J. Taiwan Inst. Chem. Eng.*, 2016, **64**, 79–88.

60 N. M. Mahmoodi and F. Najafi, Preparation of surface modified zinc oxide nanoparticle with high capacity dye removal ability, *Mater. Res. Bull.*, 2012, **47**, 1800–1809.

61 M. N. Sepehr, V. Sivasankar, M. Zarrabi and M. Senthil Kumar, Surface modification of pumice enhancing its fluoride adsorption capacity: an insight into kinetic and thermodynamic studies, *Chem. Eng. J.*, 2013, **228**, 192–204.

62 Y. S. Ho and G. McKay, Pseudo-second order model for sorption processes, *Process Biochem.*, 1999, **34**, 451–465.

63 W. J. Wber and J. C. Morris, *Proceedings of the International Conference on Water Pollution Symposium*, Pergamon Press, Oxford, New York, 1962.

64 F. A. Batzias and D. K. Sidiras, Dye adsorption by prehydrolysed beech sawdust in batch and fixed-bed systems, *Bioresour. Technol.*, 2007, **98**, 1208–1217.

65 C. Luo, Z. Tian, B. Yang, L. Zhang and S. Yan, Manganese dioxide/iron oxide/acid oxidized multi-walled carbon nanotube magnetic nanocomposite for enhanced hexavalent chromium removal, *Chem. Eng. J.*, 2013, **234**, 256–265.

66 G. D. Halsey, The Role of Surface Heterogeneity in Adsorption, in *Advances in Catalysis*, ed. V. I. K. W. G. Frankenburg and E. K. Rideal, Academic Press, 1952, pp. 259–269.

67 T. G. Venkatesha, R. Viswanatha, Y. Arthoba Nayaka and B. K. Chethana, Kinetics and thermodynamics of reactive and vat dyes adsorption on MgO nanoparticles, *Chem. Eng. J.*, 2012, **198–199**, 1–10.

68 S. Liu, Y. Ding, P. Li, K. Diao, X. Tan, F. Lei, Y. Zhan, Q. Li, B. Huang and Z. Huang, Adsorption of the anionic dye Congo red from aqueous solution onto natural zeolites modified with *N*,*N*-dimethyl dehydroabietylamine oxide, *Chem. Eng. J.*, 2014, **248**, 135–144.

69 O. Aksakal and H. Ucun, Equilibrium, kinetic and thermodynamic studies of the biosorption of textile dye (Reactive Red 195) onto *Pinus sylvestris* L., *J. Hazard. Mater.*, 2010, **181**, 666–672.

70 A. Xue, S. Zhou, Y. Zhao, X. Lu and P. Han, Adsorption of reactive dyes from aqueous solution by silylated palygorskite, *Appl. Clay Sci.*, 2010, **48**, 638–640.

71 A. Y. Dursun and O. Tepe, Removal of Chemazol Reactive Red 195 from aqueous solution by dehydrated beet pulp carbon, *J. Hazard. Mater.*, 2011, **194**, 303–311.

72 V. Belessi, G. Romanos, N. Boukos, D. Lambropoulou and C. Trapalis, Removal of Reactive Red 195 from aqueous solutions by adsorption on the surface of TiO_2 nanoparticles, *J. Hazard. Mater.*, 2009, **170**, 836–844.

73 F. Çiçek, D. Özer, A. Özer and A. Özer, Low cost removal of reactive dyes using wheat bran, *J. Hazard. Mater.*, 2007, **146**, 408–416.